On the TFNS Subgrid Models for Liquid-Fueled Turbulent Combustion

Nan-Suey Liu[1] and Thomas Wey[2]
NASA Glenn Research Center, Cleveland, Ohio, 44135

This paper describes the time-filtered Navier-Stokes (TFNS) approach capable of capturing unsteady flow structures important for turbulent mixing in the combustion chamber and two different subgrid models used to emulate the major processes occurring in the turbulence-chemistry interaction. These two subgrid models are termed as LEM-like model and EUPDF-like model, respectively. Two-phase turbulent combustion in a single-element lean-direct-injection (LDI) combustor is calculated by employing the TFNS/LEM-like approach as well as the TFNS/EUPDF-like approach. Results obtained from the TFNS approach employing these two different subgrid models are compared with each other, along with the experimental data, followed by more detailed comparison between the results of an updated calculation using the TFNS/LEM-like model and the experimental data.

Acronym

CFD = computational fluid dynamics
DNS = direct numerical simulation
LES = large-eddy simulation
RANS = Reynolds-averaged Navier-Stokes approach
URANS = unsteady RANS
TFNS = time-filtered Navier-Stokes approach
SGS = subgrid scale
SFC = subfilter component
FCP = filtering-control parameter
LEM = linear-eddy mixing
EUPDF = Eulerian probability density function
LDI = lean-direct injection
VBB = vortex-breakdown bubble
PVC = precession vortex core

1.0 Introduction

Together with rig testing and diagnostics, combustion CFD is now a major tool for combustion technology development. It is being used to complement, and sometimes to substitute the rig test. This leads to reduced costs, deepened insight, and improved foresight. Nevertheless, high-fidelity simulation of liquid combustion in practical engineering devices remains an elusive target in spite of significant advances in combustion modeling and simulation over the past decade. The main difficulty lies in the fact that combustion operates at the intersection of fluid dynamics, fuel chemistry, and multi-phase physics. Consequently, in addition to high-fidelity models for turbulence, chemical kinetics, and liquid fuel atomization and transport, models for accurately accounting for their interactions also are required. Furthermore, these intricate physical and chemical phenomena are present throughout a broad range of time scales and length scales in engineering devices.

Some of these modeling and simulation issues are discussed in the next section, followed by a description of the TFNS formulation for two-phase flow and the subfilter closure models in Section 3. In Section 4, we describe the estimation of the filtered, chemical-reaction source terms via two different subgrid models of turbulence-chemistry

---

[1] Research Aerospace Engineer, Combustion Branch, Associate Fellow AIAA.
[2] Research Aerospace Engineer, Combustion Branch, Member AIAA.

interaction in the framework of TFNS. In Section 5, we summarize the experimental setup and the computational set up employed to assess the TFNS/LEM-like and TFNS/EUPDF-like approaches. This is followed by presenting some of the computational results in Section 6 and concluding remarks in Section 7.

2.0 Liquid-Fueled Turbulent Combustion Modeling Challenges

The most accurate and straightforward numerical approach to fluid flow problems is to solve the Navier-Stokes equations without filtering and approximation, other than numerical discretizations, whose errors are to be controlled by highly accurate numerical schemes. This approach is known as the direct numerical simulation (DNS). Presently, due to its demand on computing resources, DNS is not yet practical for engineering applications. Besides, even when the governing equations are solved directly in DNS, the use of models to accommodate the multiphase formulation and interaction is still unavoidable. Modeling and simulation of liquid-fuel injection and spray transport is a very difficult task. In fact, many existing large-eddy simulation (LES) of spray flow and combustion invoke the same liquid-phase models as those used in the traditional Reynolds-averaged Navier-Stokes (RANS) approach, with a subgrid-scale (SGS) model used for the gas-phase turbulence. LES uses spatial filtering to explicitly account for flow structures larger than the filter width, the filtering in LES leads to unknown terms in the filtered equations, and these so-called SGS terms need to be modeled to form a closed set of the fluid flow governing equations. For chemically reacting flow, evaluation of the filtered term arising from the production and destruction of chemical species is quite challenging, whether the approach is the traditional RANS or LES, as the turbulence-chemistry interaction is present throughout the turbulence spectrum. Furthermore, in the case of liquid-fueled combustion, the flame structure is usually very complex and locally (both in space and time) can range from nonpremixed to premixed burning.

In any event, a prerequisite for accurate simulation of turbulent combustion in the combustor is the ability of the turbulence model to capture the unsteady turbulent structures responsible for the fuel-oxidizer-products mixing. Approaches such as the large-eddy simulation (LES) and the time filtered Navier-Stokes simulation (TFNS) are capable of capturing the dynamically important, unsteady turbulent flow structures. In the framework of the conventional LES, the filtered equations are established by applying a spatial filter to the exact form of the governing equations. The filter width is typically the local grid size; in addition, the eddy viscosity uses the local grid size as a model parameter. Therefore, the grid resolution and the model fidelity are formally linked, and, in principle, a grid independent solution cannot be reached. An explicitly filtered LES approach can be used to mitigate this issue (Ref. 1), and this is an area which needs further development. Last but not the least, the need to use fine grids when performing LES is of paramount importance, because, in LES, the subfilter field coincides with the subgrid field.

In the framework of TFNS, the filtered equations are established by applying a temporal filter to the exact form of the governing equations. The filter width does not relate to the time step of the numerical solution, and the eddy viscosity contains a so called filtering-control parameter, which is nominally defined as the ratio of a (conceptual) temporal filter width to a characteristic integral time scale of the turbulent flow. Since the grid resolution and the model fidelity are not formally linked, in principle, a grid independent solution can be attained. It should be pointed out that TFNS is not LES, nor hybrid RANS/LES, nor, in general, unsteady RANS (URANS). When performing TFNS, grids should numerically support the spatial gradients of the filtered variables. Since the smoothness of these spatial gradients correlates to the specified value of the filtering-control parameter, numerical accuracy demands that the employed grid sizes and grid distribution be consistent with the specified value of the filtering-control parameter. This is a reflection of the characteristic of TFNS, i.e., the subfilter field is not the subgrid field. And unlike the scale adaptive schemes typically adopted in the hybrid RANS/LES, we do not adapt the eddy viscosity according to the local grid resolution. The TFNS approach is summarily presented in Section 3.

An integral part of turbulent combustion is the turbulence-chemistry interaction. As mentioned above, this interaction occurs throughout the entire turbulence spectrum, and the flames usually exhibit multiregime behavior. In any approach based on filtered transport equations, whethere it is LES or TFNS or RANS, evaluation of the filtered terms arising from the production and destruction of chemical species is quite challenging. To this end, various algorithms and models have been reported in the open literature. Here, in Section 4, we present two different subgrid models developed for the TFNS approach.

Surrogate of the targeted fuel, e.g. the Jet-A, and its transport properties as well as its chemical kinetics should also be determined. Fuel chemistry models ranging from global reduced mechanism involving a few species and reaction steps to detailed mechanism involving several hundreds of species and reaction steps exist. Global reactions are computationally less intensive, but they lack emissions and extinction information. Kinetics calculations using detailed mechanism consume long CPU time as well as large computer memory; hence, they are rarely, if ever, performed on the flight during the simulation. Typically, libraries of pre-computed tables are established by using detailed mechanism, then, linked to the simulation through interpolation procedure. Tabulation strategy such as the artificial neural network (ANN) has been used to further speed up the kinetics calculations while reducing the memory requirement.

For liquid-fueled combustion, models for primary atomization, secondary droplet breakup, droplet vaporization, and droplet transportation are needed. The performances of these models directly impact the local fuel vapor distribution in the computed flow field, and can play a major role in the overall accuracy of the simulation.

For design and analysis of practical engineering devices, modeling the geometry is as important as modeling the physical and chemical processes. Accurate simulation of turbulent combustion in combustors requires precise representation of various geometrical features and high-quality mesh distribution in critical regions to numerically capture the controlling flow structures and dynamical processes.

3.0 Mathematical Formulation

The conservation equations for compressible reacting flow are solved using the TFNS approach. To simulate spray combustion, Lagrangian droplet model is concurrently solved with the Eulerian gas phase. In the following, we will briefly describe the definitions of time-filtered quantity, the gas-phase equations, and the coupling between the gaseous field and the spray field. We will then make general comments on the spray modeling without presenting the liquid-phase equations, followed by comments on the geometry modeling.

3.1 Time-Filtered Quantities $\overline{\phi}(\boldsymbol{x},t)$ and $\widetilde{\phi}(\boldsymbol{x},t)$

In the case of compressible turbulent flow, we often use two distinct but closely related time-filtered quantities. One is denoted by $\overline{\phi}(\boldsymbol{x},t)$, which is defined as

$$\overline{\phi}(\boldsymbol{x},t) = \int_{-\infty}^{+\infty} \phi(\boldsymbol{x},t')G(t-t')\,dt' \tag{1}$$

The integration is over the entire time domain $-\infty < t' < +\infty$. Where ϕ is an unfiltered turbulent variable and $G(t-t')$ is a temporal filter with a constant filter width Δ_T. Furthermore, this temporal filter satisfies the following conditions:

$$\int_{-\infty}^{+\infty} G(t-t')\,dt' = 1 \tag{2}$$

$$\int_{-\infty}^{+\infty} \phi(\boldsymbol{x},t')G(t-t')\,dt' = \phi(\boldsymbol{x},t), \quad \text{as } \Delta_T \to 0 \tag{3}$$

The other filtered quantity is denoted by $\widetilde{\phi}(\boldsymbol{x},t)$, which is defined as

$$\widetilde{\phi}(\boldsymbol{x},t) = \frac{\overline{\rho\phi}}{\overline{\rho}} \tag{4}$$

That is, $\widetilde{\phi}(x,t)$ is determined by the familiar Favre filtering, which is density-weighted.

3.2 Gas-Phase TFNS Equations

Applying a temporal filter with a constant filter width to the exact equations of conservation of mass, momentum, energy, and chemical species, as well as the equation of state, the following filtered governing equations in the TFNS framework are obtained,

$$\frac{\partial\overline{\rho}}{\partial t}+\frac{\partial\,\overline{\rho}\widetilde{U}_j}{\partial x_j}=\tilde{\dot{\rho}}_{liq} \tag{5}$$

$$\frac{\partial\overline{\rho}\widetilde{U}_i}{\partial t}+\frac{\partial}{\partial x_j}\left[\overline{\rho}\tilde{U}_i\tilde{U}_j+\overline{P}\,\delta_{ij}-\overline{\tau}_{ij}+\tau_{ij}^{sfc}\right]=\tilde{\dot{F}}_{i,liq} \tag{6}$$

$$\frac{\partial\overline{\rho}\,\widetilde{E}}{\partial t}+\frac{\partial}{\partial x_i}\left[\left(\overline{\rho}\widetilde{E}+\overline{P}\right)\widetilde{U}_i+\overline{q}_i-\overline{\tau}_{ji}\,\widetilde{U}_j+E_i^{sfc}+II_i^{sfc}+\sigma_i^{sfc}\right]=-S_k+\tilde{\dot{Q}}_{liq} \tag{7}$$

$$\frac{\partial\overline{\rho}\widetilde{Y_m}}{\partial t}+\frac{\partial}{\partial x_i}\left[\overline{\rho}\widetilde{Y_m}\widetilde{U}_i-\overline{g}_{mi}+F_{mi}^{sfc}\right]=\overline{\rho}\tilde{S}_m+\tilde{\dot{\rho}}_{m,liq} \tag{8}$$

$$\overline{P}=\overline{\rho}R_u\sum_{m=1}^{N_s}\frac{\tilde{Y}_m\tilde{T}}{MW_m}+\overline{\rho}R_u\sum_{m=1}^{N_s}T_m^{sfc} \tag{9}$$

where $\overline{\rho}$ is the filtered mass density, $\tilde{U}_i$ is the filtered velocity vector, $\overline{P}$ is the filtered pressure determined from the filtered equation of state, $\tilde{E}$ is the filtered total energy per unit mass, $\overline{\tau}_{ij}$ is the filtered viscous stress, $\overline{q}_i$ is the filtered heat flux vector, and S_k is the source term due to the subfilter kinetic energy. In addition, $\tilde{Y}_m$ is the filtered mass fraction of the m-th species, $\overline{g}_{mi}$ is the filtered mass flux vector of the m-th species. $\tilde{S}_m$ is the filtered reaction-source term of the m-th species, MW_m is the molecular weight of the m-th species, R_u is the universal gas constant, and $\tilde{T}$ is the filtered temperature, N_s is the total number of species. Subscript 'liq' denotes source term due to the liquid phase. Super script 'sfc' denotes the subfilter component (SFC) which requires closure.

The filtered viscous stress tensor, the filtered heat flux vector, and the filtered mass flux vector of the m-th species are approximated by

$$\overline{\tau}_{ij}=2\overline{\mu}\tilde{S}_{ij}-\frac{2}{3}\overline{\mu}\tilde{S}_{kk}\delta_{ij} \tag{10}$$

$$\overline{q}_i=-\overline{\kappa}\frac{\partial\widetilde{T}}{\partial x_i}-\sum_{m=1}^{N_s}\overline{\rho}\,\overline{D}_m\tilde{h}_m\frac{\partial\tilde{Y}_m}{\partial x_i}+\sum_{m=1}^{N_s}q_{i,m}^{sfc} \tag{11}$$

$$\bar{g}_{mi} = \bar{\rho}\bar{D}_m \frac{\partial \tilde{Y}_m}{\partial x_i} \tag{12}$$

where $\tilde{S}_{ij}$ is the filtered strain-rate tensor, and $\tilde{h}_m$ is the filtered specific enthalpy of the m-th species. Here, the molecular viscosity ($\bar{\mu}$) is approximated by the Sutherland's law based on the filtered temperature ($\tilde{T}$). In addition, the thermal conductivity ($\bar{\kappa}$) and the diffusion coefficient of the m-th species are approximated by

$$\bar{\kappa} = \bar{\mu}\bar{c}_p / P_r$$

$$\bar{D}_m \approx \frac{\bar{\mu}}{\bar{\rho}\, Sc_T}$$

where $\bar{c}_p$ is the specific heat at constant pressure for the gaseous mixture, P_r is the Prandtl number, and Sc_T is the turbulent Schmidt number.

The SFC terms that require closure are

$$\tau_{ij}^{sfc} \equiv \bar{\rho}(\widetilde{U_i U_j} - \tilde{U}_i \tilde{U}_j)$$

$$q_{i,m}^{sfc} \equiv \overline{h_m D_m \frac{\partial Y_m}{\partial x_i}} - \tilde{h}_m \bar{D}_m \frac{\partial \tilde{Y}_m}{\partial x_i}$$

$$E_i^{sfc} \equiv \bar{\rho}\left(\widetilde{EU_i} - \tilde{E}\tilde{U}_i\right)$$

$$II_i^{sfc} \equiv \overline{PU_i} - \bar{P}\tilde{U}_i$$

$$\sigma_i^{sfc} \equiv \widetilde{U_j \tau_{ji}} - \tilde{U}_j \bar{\tau}_{ji}$$

$$F_{mi}^{sfc} \equiv \bar{\rho}\left(\widetilde{U_i Y_m} - \tilde{U}_i \tilde{Y}_m\right)$$

$$T_m^{sfc} \equiv \widetilde{Y_m T} - \tilde{Y}_m \tilde{T}$$

In the present study, we neglect terms such as $q_{i,m}^{sfc}$, II_i^{sfc}, and T_m^{sfc}. The closure for the rest of the SFC terms is described below.

3.2.1 Momentum Transport Closure

A general constitutive relationship between subfilter turbulent stresses and filtered strain rate (Ref. 2) leads to a nonlinear model for τ_{ij}^{sfc}, i.e.

$$
\begin{aligned}
\tau_{ij}^{sfc} &= -2\,\bar{\rho}\,\nu_T\left(\tilde{S}_{ij} - \delta_{ij}\tilde{S}_{kk}\big/3\right) + \frac{2}{3}\bar{\rho}\,k\,\delta_{ij} \\
&\quad - A_3\,f\,\bar{\rho}\frac{k^3}{\varepsilon^2}\left(\tilde{S}_{ik}\tilde{\Omega}_{kj} - \tilde{\Omega}_{ik}\tilde{S}_{kj}\right) \\
&\quad + 2A_5\,f\,\bar{\rho}\frac{k^4}{\varepsilon^3}\left[\tilde{\Omega}_{ik}\tilde{S}_{kj}^2 - \tilde{S}_{ik}^2\tilde{\Omega}_{kj} + \tilde{\Omega}_{ik}\tilde{S}_{km}\tilde{\Omega}_{mj} - \tilde{\Omega}_{kl}\tilde{S}_{lm}\tilde{\Omega}_{mk}\delta_{ij}/3 + II_s(\tilde{S}_{ij} - \delta_{ij}\tilde{S}_{kk}\big/3)\right],
\end{aligned}
\tag{13}
$$

where, $\tilde{S}_{ij} = \left(\widetilde{U}_{i,j} + \widetilde{U}_{j,i}\right)\big/2$, $\tilde{\Omega}_{ij} = \left(\widetilde{U}_{i,j} - \widetilde{U}_{j,i}\right)\big/2$, $II_s = \left(\tilde{S}_{kk}\tilde{S}_{mm} - \tilde{S}_{kl}\tilde{S}_{lk}\right)\big/2$.

The model coefficients C_μ, A_3 and A_5 are constrained by the realizability condition and the rapid distortion theory limit. They are formulated as (Ref. 3):

$$
C_\mu = \frac{1}{4.0 + A_s\dfrac{k}{\varepsilon}U^*}, \quad A_3 = \frac{\sqrt{1.0 - A_s^2 C_\mu^2\left(\dfrac{k}{\varepsilon}S^*\right)^2}}{0.5 + 1.5\dfrac{k^2}{\varepsilon^2}\Omega^* S^*}, \quad A_5 = \frac{1.6\,C_\mu\bar{\rho}\dfrac{k^2}{\varepsilon}}{\bar{\rho}\dfrac{k^4}{\varepsilon^3}\dfrac{7S^*S^* + \Omega^*\Omega^*}{4}},
$$

in which,

$$
A_s = \sqrt{6}\cos\varphi, \quad \varphi = \frac{1}{3}\arccos\left(\sqrt{6}\,W^*\right), \quad W^* = \frac{S_{ij}^* S_{jk}^* S_{ki}^*}{(S^*)^3},
$$

$$
U^* = \sqrt{(S^*)^2 + (\Omega^*)^2}, \quad S^* = \sqrt{S_{ij}^* S_{ij}^*}, \quad \Omega^* = \sqrt{\tilde{\Omega}_{ij}\tilde{\Omega}_{ij}}, \quad S_{ij}^* = \tilde{S}_{ij} - \frac{1}{3}\delta_{ij}\tilde{S}_{kk}
$$

The coefficient f is a function of the filtering-control parameter (FCP) which is nominally defined as the ratio of a (conceptual) time filter width Δ_T to an integral time scale T, i.e., FCP = Δ_T / T. Furthermore (Ref. 4),

$$
f\left(\frac{\Delta_T}{T}\right) \approx 2\left(\frac{\Delta_T}{T}\right) - \left(\frac{\Delta_T}{T}\right)^2 \tag{14}
$$

By definition, the value of the parameter FCP and the value of the coefficient f are always between 0 and 1.

This model uses the concept of subfilter eddy viscosity which is defined as

$$
\nu_T = f \cdot C_\mu \cdot k^2 / \varepsilon
$$

$$
\mu_T = \bar{\rho}\,\nu_T
$$

Here, the subfilter turbulent kinetic energy and its dissipation rate (k, ε) are supplied by the following model equations:

$$\frac{\partial}{\partial t}\bar{\rho}k + \frac{\partial}{\partial x_i}\left[\bar{\rho}\tilde{u}_i k - \left(\bar{\mu} + \frac{\mu_T}{\sigma_k}\right)\frac{\partial k}{\partial x_i}\right] = S_k \tag{15}$$

$$\frac{\partial}{\partial t}\bar{\rho}\varepsilon + \frac{\partial}{\partial x_i}\left[\bar{\rho}\tilde{u}_i \varepsilon - \left(\bar{\mu} + \frac{\mu_T}{\sigma_\varepsilon}\right)\frac{\partial \varepsilon}{\partial x_i}\right] = S_\varepsilon \tag{16}$$

where σ_k and σ_ε are model constants, and the source terms are given by

$$S_k = -\,\tau_{ij}^{sfc}\,\tilde{s}_{ij} - \bar{\rho}\,\varepsilon \tag{17}$$

$$S_\varepsilon = -\,C_{\varepsilon 1}\tau_{ij}^{sfc}\tilde{s}_{ij}\frac{\varepsilon}{k} - C_{\varepsilon 2}\frac{\bar{\rho}\,\varepsilon^2}{k} \tag{18}$$

where $C_{\varepsilon 1}$ and $C_{\varepsilon 2}$ are the model coefficients. We have adopted the commonly used values of $C_{\varepsilon 1}$ = 1.45 and $C_{\varepsilon 2}$ = 1.92 in the present work.

In practice, the content of the subfilter turbulent kinetic energy is regulated by the (specified) filtering-control parameter FCP. Since the subfilter turbulent kinetic energy is, by definition, a fraction of the total turbulent energy, its value should be smaller than the RANS turbulent kinetic energy.

3.2.2 Energy Transport Closure

The subfilter total energy flux, E_i^{sfc}, is also modeled using the subfilter eddy viscosity and gradient assumption, a nonlinear model is formulated as (Ref. 3)

$$E_i^{sfc} = -\kappa_T\frac{\partial \tilde{T}}{\partial x_i} - \frac{\mu_T}{\bar{\rho}}\frac{1}{\mathrm{Pr}_T}\frac{k}{\varepsilon}\left(c_1\tilde{S}_{ij} + c_2\tilde{\Omega}_{ij}\right)\frac{\partial \bar{\rho}\,\bar{c}_\upsilon\,\tilde{T}}{\partial x_j} \tag{19}$$

here, Pr_T is the turbulent Prandtl number, $\bar{c}_\upsilon$ is the specific heat at constant volume for the gaseous mixture. The coefficients c_1 and c_2 are yet to be extensively calibrated. In the current simulations they are set to be $c_1 = c_2 =$ -0.24. The subfilter thermal conductivity (κ_T) is evaluated via

$$\kappa_T = \mu_T\bar{c}_p / \mathrm{Pr}_T$$

It is noted here that the filtered total energy ($\tilde{E}$) is evaluated as

$$\tilde{E} = \tilde{e} + \frac{1}{2}\tilde{U}_i\tilde{U}_i$$

where $\tilde{e}$ is the filtered specific internal energy of the mixture. The subfilter viscous work is modeled as

$$\sigma_i^{sfc} = \tilde{U}_j \tau_{ji}^{sfc} \tag{20}$$

3.2.3 Species Transport Closure

Similar to the subfilter total energy flux, the subfilter mass flux of the m-th species is modeled as

$$F_{mi}^{sfc} = -\bar{\rho}\, Dm_T \frac{\partial \tilde{Y}_m}{\partial x_i} - Dm_T \frac{k}{\varepsilon}\left(c_1 \tilde{S}_{ij} + c_2 \tilde{\Omega}_{ij}\right)\frac{\partial \bar{\rho}\tilde{Y}_m}{\partial x_j} \tag{21}$$

with

$$Dm_T = \frac{\mu_T}{\bar{\rho} Sc_T}$$

where Sc_T is the turbulent Schmidt number.

In the present study, the filtered reaction rate of the m-th species (i.e. $\tilde{S}_m$ in Eq. (8)) is estimated via subgrid models of turbulent mixing and combustion, and these models are described in Section 4.

3.3 Coupling between Gaseous Field and Spray Field

The coupling between the gaseous and spray field is through the interphase exchange terms. The effects of the spray field on the gaseous field are accounted for via the 'liquid' source terms in the gas-phase equations (Eq. (5), Eq. (6), Eq. (7), and Eq. (8)), and they are modeled as (Ref. 5)

$$\tilde{\dot{\rho}}_{liq} = \frac{1}{V_c}\sum_k n_k \dot{m}_k \tag{22}$$

$$\tilde{\dot{F}}_{i,liq} = \frac{1}{V_c}\sum_k n_k \left(\dot{m}_k u_{ki} - \frac{4\pi}{3}\rho_k r_k^3 \frac{d\, u_{ki}}{dt}\right) \tag{23}$$

$$\tilde{\dot{Q}}_{liq} = \frac{1}{V_c}\sum_k n_k \dot{m}_k \left(h_s - \ell_{k,eff}\right) \tag{24}$$

$$\tilde{\dot{\rho}}_{m,liq} = \frac{1}{V_c}\sum_k \varepsilon_m n_k \dot{m}_k \tag{25}$$

where V_c is the volume of the computational cell, n_k is the number of droplets in the k-th drop group, $\dot{m}_k$ is the vaporization rate of droplets in the k-th group, u_{ki} is the i-th velocity component of the k-th group, ρ_k is the density of droplets in the k-th group, r_k is the droplet radius in the k-th group, h_s is the specific enthalpy at the droplet surface, $\ell_{k,eff}$ is the effective latent heat of vaporization of droplets in the k-th group, and ε_m is the fractional vaporization rate for the m-th species.

3.4 Liquid-Phase Modeling

The governing equations of the liquid phase are based on a Lagrangian formulation where the spray particle position and velocity are described by a set of ordinary differential equations. Various submodels, such as the droplet drag model and the drop vaporization model, are needed to simulate the transport of a vaporizing spray particle. The specification of the fuel injection condition plays a major role in the fidelity of the simulation. Common practice is to specify the starting droplet condition using correlations of droplet sizes calibrated by relevant experimental data. In addition to the use of correlation, various models for primary atomization and secondary droplet breakup also have been employed. A more detailed description of the liquid phase modeling and the two-way coupling between the liquid-phase and the gas-phase transport can be found in Ref. 5.

3.5 Geometry Modeling

To improve the representation of complex geometrical features and to enable high-quality mesh distribution in critical regions, we have established capabilities of generating and using arbitrary polyhedral mesh derived from hanging-node elements as well as capabilities of adaptive mesh refinement using information from the flow solutions. Description and demonstration of these capabilities can be found in Ref. 6.

4.0 Subgrid Models for Mixing and Combustion

Simulation of turbulent combustion requires modeling the effects of turbulence-chemistry interaction processes occurring throughout the entire turbulence spectrum, and various approaches have been invoked in many previous studies. Examples of these approaches include the eddy-break-up (EBU) model (Ref. 7), the thickened flame model (Ref. 8), the flamelet-based method (Ref. 9), the conditional moment closure (CMC) method (Ref. 10), the filtered mass density function/probability density function (FDF/PDF) method (Ref. 11), and the linear-eddy mixing (LEM) model (Ref. 12). Sometimes, a rudimentary model, termed here as the un-mixed (umx) model, is employed. The un-mixed model does not involve itself with the mixing processes happening within the CFD computational cells. Rather, the (highly nonlinear) filtered reaction source terms are evaluated simply by using the filterd temperature and filtered speciese mass fractions directly supplied by the solutions of the filtered governing equations.

Invoking the FDF/PDF method or the LEM model usually leads to a hybrid algorithm. The velocity and the density over the entire computational domain are obtained by solving the filtered Navier-Stokes equations via finite-difference scheme or finite-volume scheme. The scalars (i.e., the energy and the species mass fractions) over the entire computational domain are obtained by solving the FDF/PDF transport equation or the LEM transport equation via stochastical elements such as the Monte Carlo particles (in the case of FDF/PDF method) or the linear cells (in the case of LEM model), i.e., the filtered conservation equations for the scalars are not employed. Examples of hybrid LES/FDF and hybrid LES/LEM can be found in Ref. 11and Ref. 12, respectively. By their nature, both the FDF/PDF method and the LEM model can handle the multiregime flame structures, but the FDF/PDF method usually lumps the molecular diffusion and the small scale turbulence effects into a single process known as micro-mixing. An Eulerian Monte Carlo implementation of the FDF/PDF method, termed as the EUPDF model, is described in relative detail in Ref.13. Examples of hybrid RANS/EUPDF and hybrid TFNS/EUPDF can be found in Ref.14 and Ref. 15, respectively.

Under the current TFNS approach, the energy and the species mass fractions over the entire computational domain are obtained by solving the filtered conservation equations. The LEM model or the EUPDF model is used as a subgrid model for mixing and combustion to provide an estimation of the filtered reaction source terms appearing in the filtered conservation equations, and they are termed as the LEM-like model and the EUPDF-like model, respectively. More specifically, (i) instead of using the LEM model or the EUPDF model to directly establish the entire species field without actually solving the filtered conservation equations of species, the LEM model or the EUPDF model is used locally (both in space and time) to only provide approximations of filtered reaction source terms in the filtered equations which are now being solved, (ii) instead of solving the unfiltered quantities using the LEM equations or the EUPDF equations, the same mathematical forms of the LEM equations or the EUPDF equations for the unfiltered quantities are analogously adopted as a subgrid model for mixing and combustion of time-filtered scalars, with the molecular transport coefficients substituted by the ‘effective’ transport coefficients.

4.1 LEM-like Model

We have adapted the LEM model described in Ref. 12 into the current TFNS framework, and, for the reasons mentioned above, we call it LEM-like. The LEM-like model is implemented in terms of a fractional splitting technique; it is divided into a supergrid process and a subgrid process. The supergrid process emulates the convection of the scalar field by grid-resolved velocity field across the surfaces of the computational cell. The subgrid process, which occurs within each computational cell, consists of four operators: (a) (effective) molecular diffusion, (b) finite-rate chemical reaction, (c) volumetric expansion caused by the heat release, and (d) stochastic stirring due to the subgrid eddies.

4.1.1 Supergrid Process

The macro mixing of the scalars is implemented by a Lagrangian transfer of LEM elements across the surfaces of the CFD computational cells. This Lagrangian transport is known as the ‘splicing’, and each LEM element carries its own volume, filtered temperature, and filtered species density. Referring to Fig. 1, for example, the outward mass through the right side of a cell computed from filtered velocity and density is equivalent to 1.5 LEM elements and colored in red. The outward mass through the bottom side of the mesh is equivalent to 2.5 LEM elements and colored in magenta. Similarly, the inward mass through the top and left sides of the mesh are equivalent to 6 LEM elements. Splicing will result in 14 LEM elements in this computational cell. In general, splicing will cause different computational cell to have different number of LEM elements. To avoid programming complexities in a parallel environment, the LEM domain is re-gridded to have the same fixed number of elements, and each element is of the same volume. Conservation of mass is maintained during the re-gridding procedure.

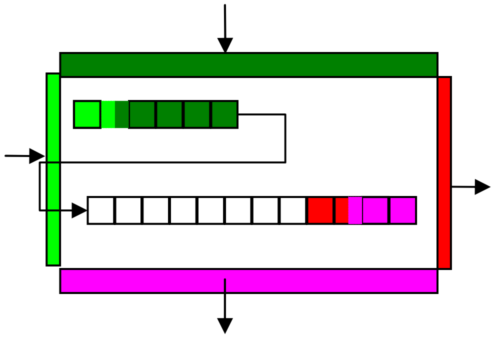

Arrows -- Convection direction
Initial number of lumps – 12
Light Green – inward mass (1.5)
Dark Green – inward mass (4.5)
Red – outward mass (1.5)
Magenta – outward mass (2.5)
Current number of lumps -- 14
Final number of lumps will become 12 after re-gridding via equalizing the volume.

Figure 1. Schematic illustrating the splicing algorithm used for scalar convection in the LEM-like model.

4.1.2 Subgrid Process

Within each CFD computational cell, a one-dimensional domain consisting of a fixed number of LEM elements is employed, the governing equations have the following form:

$$\bar{\rho}\frac{\partial \tilde{Y}_m}{\partial t} = F_{\tilde{Y}_m, stirring} + \frac{\partial}{\partial s}\left(\bar{\rho} D_{m,eff}\frac{\partial \tilde{Y}_m}{\partial s}\right) + \bar{\rho}\,\dot{\omega}_m(\tilde{Y}_1, \tilde{Y}_2, \cdots, \tilde{Y}_{N_s}) \tag{26}$$

$$\overline{\rho c}_p \frac{\partial \tilde{T}}{\partial t} = F_{\tilde{T}, stirring} + \sum_{m=1}^{N_s}\left(\overline{\rho c}_{pm} D_{m,eff}\frac{\partial \tilde{Y}_m}{\partial s}\frac{\partial \tilde{T}}{\partial s}\right) + \frac{\partial}{\partial s}\left(\kappa_{eff}\frac{\partial \tilde{T}}{\partial s}\right) - \sum_{m=1}^{N_s}\bar{\rho}\tilde{h}_m\,\dot{\omega}_m \tag{27}$$

where $F_{\tilde{Y}_m, stirring}$ and $F_{\tilde{T}, stirring}$ represent the subgrid turbulent mixing, and they are accounted for by employing a stochastic rearrangement of the LEM elements, known as the triplet mapping, more details about this mapping procedure can be found in Ref. 12. Here, $D_{m,eff}$ is the effective mass diffusion coefficient, κ_{eff} is the effective heat conductivity, and $\dot{\omega}_m(\tilde{Y}_1, \tilde{Y}_2, \cdots, \tilde{Y}_{N_s})$ indicates that the reaction kinetics of unfiltered species mass fractions is formally used for the reaction kinetics of filtered species mass fractions.

The solution of the above one-dimensional LEM-like equations over *NLEN* elements gives a subgrid field of $\tilde{Y}_m$, namely, $\tilde{Y}_m^{l=1}, \tilde{Y}_m^{l=2}, \cdots, \tilde{Y}_m^{l=NLEN}$. Their average, $\tilde{Y}_m^{LEM}(t+\Delta t)$, provides a prediction of $\tilde{Y}_m(t+\Delta t)$ at the center of the computational cell. This predicted value is then used to construct an estimaion of the filtered source term ($\tilde{S}_m$) needed to solve Eq. (8). In the current study, the estimation is via

$$\tilde{S}_m = \frac{\tilde{Y}_m^{LEM}(t+\Delta t) - \tilde{Y}_m^{TFNS}(t)}{\Delta t}$$

where $\tilde{Y}_m^{TFNS}(t)$ is the TFNS solution of the (filtered) species mass fraction at the computational cell center.

4.2 EUPDF-like Model

We have adapted the EUPDF model described in Ref. 13 into the current TFNS framework, and, for the reasons mentioned above, we call it EUPDF-like. The EUPDF-like model is implemented by making use of an operator splitting scheme; it is divided into a supergrid process and a subgrid process. The supergrid process accounts for the convection as well as the diffusion of the scalar field by grid-resolved velocity field across the surfaces of the computational cell. The subgrid process, which occurs within each computational cell, consists of two operators: (a) micro mixing, and (b) finite-rate chemical reaction.

4.2.1 Supergrid Process

The grid-resolved convection and diffusion of the scalar field is implemented in an Eulerian fashion. Referring to Figure 2, unlike the LEM splicing algorithm, the Eulerian convection and diffusion process is achieved through the content replacement of particles, as each Monte Carlo particle carries the information of the mass fraction of species, the enthalpy, the temperature, but not the volume. For example, the outward mass through the right side of a cell, computed from the grid-resolved velocity and density; and normalized by the mass in the cell, is equal to 5% and colored in red. The outward mass through the bottom side of the mesh is equal to 10% and colored in magenta. Similarly, the inward mass through the top and left sides of the mesh are equivalent to 40% and colored in dark and light green. If the total number of the particles is 20 in this cell, then one particle (5% of 20) will be randomly selected from its right adjacent cell, and its contents are copied to one randomly selected particle in the current cell. The same procedure is applied to other particles in colors. For those remaining particles (45% here) the contents are randomly shuffled within the cell.

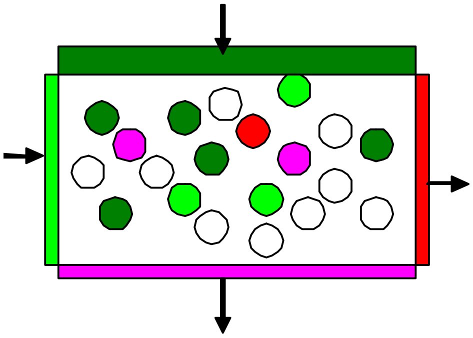

Arrows -- Convection direction
Light Green – inward mass (15%=3)
Dark Green – inward mass (25%=5)
Red – outward mass (5%=1)
Magenta – outward mass (10%=2)
Number of Monte Carlo particles – 20
Contents of randomly selected particles are replaced by those of randomly selected particles from adjacent cells.

Figure 2 Schematic illustrating the process of the convection and diffusion of the scalar field in the EUPDF-like model

4.2.2 Subgrid Process

Within each CFD computational cell, an ensemble of Monte Carlo particles is employed. The number of particles within each CFD computational cell is fixed. These particles are notional and, for each particle, the governing equations have the following form:

$$\frac{\partial \tilde{Y}_m}{\partial t} = -c_\phi \Omega (\tilde{Y}_m - < \tilde{Y}_m >) + \dot{\omega}_m (\tilde{Y}_1, \tilde{Y}_2, \cdots, \tilde{Y}_{N_s}) \tag{28}$$

$$\frac{\partial \tilde{h}}{\partial t} = -c_\phi \Omega (\tilde{h} - < \tilde{h} >) \tag{29}$$

where c_ϕ is an empirical constant , Ω is a measure of the turbulence frequency (see, for example, Ref. 15), and < > denotes the ensemble average over the Monte Carlo particles in a given CFD computational cell. In addition, $\dot{\omega}_m (\tilde{Y}_1, \tilde{Y}_2, \cdots, \tilde{Y}_{N_s})$ indicates that the reaction kinetics of unfiltered species mass fractions is formally used for the reaction kinetics of filtered species mass fractions.

The solution of the above EUPDF-like equations over *NPAR* particles gives a subgrid field of $\tilde{Y}_m$, namely, $\tilde{Y}_m^{l=1}, \tilde{Y}_m^{l=2}, \cdots, \tilde{Y}_m^{l=NPAR}$. Their average, $\tilde{Y}_m^{EUPDF}(t + \Delta t)$, provides a prediction of $\tilde{Y}_m(t + \Delta t)$ at the center of the computational cell. This predicted value is then used to construct an estimation of the filtered source term ($\tilde{S}_m$) needed to solve Eq. (8). In the current study, the estimation is via

$$\tilde{S}_m = \frac{\tilde{Y}_m^{EUPDF}(t + \Delta t) - \tilde{Y}_m^{TFNS}(t)}{\Delta t}$$

where $\tilde{Y}_m^{TFNS}(t)$ is the TFNS solution of the (filtered) species mass fraction at the computational cell center.

5.0 Experimental and Computational Setup

The modeling-and-simulation capabilities outlined in the previous sections are embodied in a NASA in-house code known as the National Combustion Code (Refs. 16-22). Its target application is for low-emissions, fuel-flexible combustors, including the lean-direct-injection (LDI) combustors.

A typical single-element LDI combustor is illustrated in Fig. 3. More detailed description of the combustor geometry and the test rig can be found in Ref. 23. Each element consists of an air passage with an upstream air swirler and a converging-diverging venturi section. The fuel is injected through the center of the swirler and the fuel tip is at the throat of the venturi. The air swirler has six helical, axial vanes with downstream vane angles of 60-degree. The air then dumps into a combustion chamber with a square cross-section. Velocity measurements were taken with a two-component Laser Doppler Velociometry (LDV) system, temperature measurements were taken with thermocouples, emissions data were gathered via an isokinetic probe and gas analyzer, and droplet data were collected with a Phase Doppler Particle Analyzer (PDPA). The temperature measurements may suffer from radiation and conduction loss and other loss due to the presence of liquid droplets. In regions close to the dump plane, the gas-phase velocity measurements may suffer from interferences caused by the presence of small liquid particles.

The extent of the computational domain is shown in Fig. 3. At the air inflow boundary, the air flow speed is 20.14 m/s, the density is 1.19 kg per cubic meter, and the static temperature is 294.28 °K. The operating pressure of the combustor is approximately 1 atm, and the measured pressure drop (as a percentage of the air inlet pressure) during the experiments was measured at 4 %. At the combustor chamber exit, an outlet boundary condition facilitating the convection of pressure disturbances out of the computational domain is applied (Ref. 24). Adiabatic and non-slip conditions, along with a generalized wall function (Ref. 25), are imposed on the wall surfaces.

The liquid fuel is injected at 0.415 g/s, which gives a global equivalence ratio of 0.75. The specification of the starting condition for the fuel spray is critical for high-fidelity simulations. In this study, the following droplet size distribution is used at the injection point (Ref. 5):

$$\frac{dn}{n} = 4.21\times 10^{6}\left[\frac{d}{d_{32}}\right]^{3.5} e^{-16.98\left(\frac{d}{d_{32}}\right)^{0.4}} \frac{dd}{d_{32}} \tag{30}$$

where n is the total number of the droplets and dn is the number of droplets in the size range between d and $d + dd$. This correlation requires specifying a Sauter mean diameter, d_{32} , as well as the number of droplet groups. In the present simulation, the Sauter mean diameter is set to be 50 microns, the number of injected droplet groups is set to be 10. At each injection event, a total of 240 spray particles enter into the computational domain at a point located in the immediate neighborhood of the injector tip. The magnitude of the droplet injection velocity is specified to be 12 m/s. The hollow spray cone has a cone angle of 90 degree with a 30-degree half-cone angle. Subsequently, these starting droplets will undergo evaporation, but without experiencing secondary breakup.

In this study, the liquid fuel $C_{12}H_{23}$ is adopted as the surrogate for the experimental Jet-A fuel, and a single-step, five-species global reduced mechanism (see e.g. Ref. 26) is employed for the chemical reactions.

Table 1 Single Step (Global) Chemistry Model.

	Reaction	**A (mole – cm – sec– K)**	**n**	**E (cal/mole)**
1	**4 C12H23 + 71 O2 => 48 CO2 + 46 H2O** *GLO / C12H23 0.10 /* *GLO / O2 1.65 /*	8.60E+11	0.00	3.00E+4

The computational domain consists of approximately 862,000 hexahedral elements. Current TFNS (with FCP = 0.255) solutions are obtained by an iteratively implicit, finite-volume scheme that is (nominally) second-order accurate in space and time. The LEM-like equations are solved using a standard fractional splitting, finite-difference scheme, and 24 LEM elements per CFD computational cell are employed. The EUPDF-like equations are solved by an operator splitting scheme, and 24 Monte Carlo particles per CFD computational cell are used. The solution for the ordinary differential equations of spray particle position, size, and velocity are advanced via a second-order accurate Runge-Kutta method.

6.0 Results

While recognizing that the inherent uncertainties in the current models of liquid fuel atomization/injection, fuel evaporation, and fuel chemistry often can be overwhelming, this LDI burner and its measured data has been used to assess as well as to guide the development of modeling-and-simulation capabilities for two-phase turbulent combustion in LDI combustors. Results from the RANS approach were reported in Ref. 26 and Ref. 27. Results from the LES/LEM approach were presented in Ref. 12. Results from the LES/flamelet approach were described in Ref. 9. And results from TFNS/EUPDF were shown in Ref.15. In the following, some of the results obtained by the TFNS/EUPDF-like approach and the TFNS/LEM-like approach are presented.

First of all, it is noted here that the TFNS results of non-reacting flow and their comparison with the experimental data can be found in Ref. 28. They reveal the major flow structures in the LDI combustor. Fig. 4 is a snapshot of the unsteady flow field. Embedded in this figure are the instantaneous iso-surface of the zero axial velocity component colored by the effective eddy viscosity and six instantaneous stream lines emanating from the upstream of the swirler, going through the converging-diverging nozzle, then passing through the combustion chamber. Major flow structures in the LDI combustor are visualized via the iso-surface of the zero axial velocity and the iso-surface of a relatively low pressure. The iso-surface of the zero axial velocity is also known as the vortex-breakdown bubble (VBB). The iso-surface of a sufficiently low pressure captures the precession vortex core (PVC). Fig. 5 is a snapshot of the PVC and VBB. The dark blue region is a vortex core, which is formed near the venturi throat and extends into the combustor chamber. This spiraling vortex core rotates and breaks, it changes in seemingly random way in space and time. The light green surfaces are the iso-surfaces of the zero axial velocity. In addition to the VBB, there are some small structures near the dump plane and in the corner region. Fig. 6 shows the instantaneous streamlines around the PVC, they start from the upstream of the swirler, and yield a complex, seemingly random pattern. Some of them spiral around the dark blue surface indicating that the dark blue region is indeed a vortex core. As demonstrated in Ref. 12, the dynamics of the PVC and the VBB, as well as their interactions, are critical to the fuel-air mixing and the flame stability in the LDI combustors.

Subsequently, the same grid is used for the two-phase reacting flow calculations, and Fig. 7 is a snapshot of the fuel-droplet distribution. The performance of the turbulence-chemistry interaction models is at first highlighted in terms of the contours of the computed temperature field, followed by comparisons of averaged temperature and averaged velocity at several locations. In addition, time history of flow variables collected at a ‘probe’ location is used to illustrate the unsteady features from using different subgrid models.

The center-plane (z=0) temperature field from the LEM-like model, the EUPDF-like model, and the un-mixed (umx) model is compared in Fig. 8. In the case of the un-mixed model and the EUPDF-like model, the filtered temperature shown is an average over 10000 time-steps (i.e., 0.01 seconds). In the case of the LEM-like model, the filtered temperature shown is an average over 5000 time-steps (i.e., 0.005 seconds). The features of the averaged temperature field obtained by using the LEM-like model are closer to what is typically observed in the experiments, as compared to the un-mixed and the EUPDF-like models.

Comparisons of averaged temperature and averaged velocity at several locations are shown from Fig. 9 to Fig. 13. They are averages over 50,000 time-steps (i.e., 0.05 seconds). The centerline averaged temperature and the centerline averaged axial velocity are given in Fig. 9 and Fig. 10, respectively. Fig. 11 depicts the radial profile of the averaged temperature at 10 mm downstream of the dump plane. The radial profiles of the averaged axial velocity and the averaged azimuthal velocity at 15 mm downstream of the dump plane are presented in Fig. 12 and Fig. 13, respectively.

Fig. 14, Fig. 15 and Fig. 16 illustrate the time history of the gage pressure, the temperature and the axial velocity sampled over 50,000 time-steps at a centerline location which is 7.8 mm downstream of the dump plane, obtained by using the EUPDF-like model. Their counterparts obtained by using the LEM-like model are shown in Fig. 17, Fig. 18 and Fig. 19. It is quite clear that the EUPDF-like model is prone to yield ‘noisy’ results. These noises are numerical artifacts caused by the nature of the Monte Carlo process.

Based on the above comparison, subsequent investigation has been focused on the results from the LEM-like model, and new sets of calculations using an updated version of the National Combustion Code (NCC) have been carried out. This NCC version contains bug fixes and newly implemented spray-wall interaction models. One set of computed data is examined here. The sampling duration of this set is 0.1 second (from time-step 430,001 to time-step 530,000), and various time averages are constructed by averaging over these 100,000 time-steps.

In the following, comparisons between time averages of filtered quantities and experimental mean values are presented. The discrepancies are due to a variety of reasons. In addition to the obvious computational reasons such as the grid resolution and model fidelity, the measurement errors aggravated by the presence of liquid droplets also play an appreciable role.

The averaged temperature along the center line downstream of the dump plane (located at x=0.0072 m) is shown in Fig. 20. Near the dump plane, the significant causes of the discrepancy are the spray injection model, droplet vaporization model, turbulent combustion model, as well as the radiation and conduction loss of the thermocouples. Further downstream, the subgrid model for turbulent mixing plays a major role. Fig. 21 presents the averaged axial velocity along the combustor center line. In the immediate neighborhood of the dump plane, there was experimental difficulty in sorting the seeder particles used in the LDV from the small yet high axial-momentum spray particles. In addition, computational heat-release tied to the spray transport and combustion model is another cause of the discrepancy. These factors also contribute to the discrepancies between the computational data and the experimental data shown in Fig. 22, Fig. 23 and Fig. 24. Fig. 22 is the radial profile of the averaged temperature at 5 mm downstream of the dump plane. The computational temperature is the pure gas temperature, however, the measured temperature consists of contributions from both pure gas and droplets. Since the sprays distribute as a hollow cone donut ring, the discrepancy in temperature is much larger in the donut ring, as compared to the discrepancy in the central region. Fig. 23 is the radial profile of the averaged axial velocity at 5 mm downstream of the dump plane. The measured gas axial velocity is all positive in the central region in spite of the recirculation zone existing at this location. This can be attributed to the presence of the small droplets which have positive velocities but are difficult to be separated from the seeding particles used in the LDV system. The radial profile of the averaged azimuthal velocity at 5 mm downstream of the dump plane is presented in Fig. 24. The presence of the small droplets which have low swirling velocities reduces the measured gas phase swirl velocity in the central region.

Radial profile of the averaged temperature at 20 mm downstream of the dump plane is shown in Fig. 25. Radial profiles of the averaged axial velocity and the averaged azimuthal velocity at 29 mm downstream of the dump plane are shown in Fig. 26 and Fig. 27, respectively. There are still discrepancies, it is apparent that grid resolution in the cross-section needs to be improved. Radial profiles of averaged temperature, averaged axial velocity, and averaged azimuthal velocity at further downstream locations are presented from Fig. 28 to Fig. 33.

Fig. 34 is the unsteady pressure recorded at a centerline point which is 7.8 mm downstream of the dump plane. Fig. 35 and Fig. 36 illustrate the intermittent feature of the mass fraction of the oxygen and the mass fraction of the fuel vapor at this 'probe' location. In Fig. 37 and Fig. 38, contour plots of time-averaged quantities in the center plane (z=0) are presented. Time-average of filtered fuel ($C_{12}H_{23}$) vapor mass fraction is shown in Fig. 37, along with two snapshot solutions. Similarly, time-average of filtered temperature, along with two snapshot solutions, are shown in Fig. 38. The time-averaged field gives the impression of an orderly, symmetric burning, while the snapshots suggest that, in parts of the flame region, the supply of fuel vapor is intermittent, and pockets of significant temperature variation exist.

7.0 Concluding Remarks

Two-phase turbulent combustion in a single-element LDI combustor has been simulated by employing the TFNS/LEM-like approach and the TFNS/EUPDF-like approach. Together with an assumed starting condition of the fuel droplets and a single-step, 5-species global reduced kinectics for the Jet-A combustion, computational results are obtained by using a computational grid consisting of approximately 862000 hexahedral cells. Results from the TFNS/LEM-like and the TFNS/EUPDF-like approaches are compared with each other, together with the experimental data. Subsequently, we have focused on the LEM-like model, as it explicitly includes the effects of molecular diffusion. These results are useful in gaining deepened insight into the unsteady physical processes in the LDI combustor. Nevertheless, in addition to the obvious numerical reasons and other model-related causes, their quantitative accuracy often suffers from the inherent uncertainties in the current spray-related models. Future plan includes replacing the present single-step combustion chemistry with a multi-step global reduced mechanism, achieving a grid-independent solution, and employing atomization as well as secondary breakup models to characterize the fuel injection processes. In regions around the injector tip, we also need to find a way to take account of the influences of the injected/dense liquid on the flow field of the co-flowing gaseous stream.

Acknowledgments

This work has been supported by the NASA Aeronautical Sciences Project under the Fundamental Aeronautics Program.

References

[1] Radhakrishnan, S. and Bellan, J., "Explicit Filtering to Obtain Grid-Spacing Independent and Discretization-Order Independent Large Eddy Simulation of Compressible Single-Phase Flow," J. Fluid Mech., vol. 697, pp. 339-435, 2012.

[2] Shih, T.-H., "Constitutive Relations and Realizability of Single-Point Turbulence Closures," *Turbulence and Transition Modeling*, *Chapter 4*, Edited by Hallback, M., Henningson, D.S., Johansson, A.V. and Alfredsson, P.H., KLUWER ACADEMIC PUBLISHERS, 1996.

[3] Shih, T.-H., "Some Developments in Computational Modeling of Turbulent Flows," Fluid Dynamic Research, Vol. 20, 1997, pp. 67-96.

[4] Shih, T.-H. and Liu, N.-S., "A Nonlinear Dynamic Subscale Model for PRNS/VLES of Internal Combustor Flows," AIAA-2009-0467, 47th AIAA Aerospace Science Meeting and Exhibit, 4-8 January, 2009, Orlando, FL.

[5] Raju, M.S., "LSPRAY-IV: A Lagrangian Spray Module," NASA/CR-2012-217294, 2012.

[6] Wey, T. and Liu, N.-S., "Updates to Simulation of a Single-Element Lean-direct Injection Combustor Using a Polyhedral Mesh Derived from Hanging-Node Elements," AIAA-2014-1385, 52th AIAA Aerospace Science Meeting and Exhibit, 13-17, January 2014, National Harbor, MD.

[7] Kirtas, M., Patel, N., Sankaran, V. and Menon, S., "Large-eddy Simulation of a Swirl-stablized, Lean Direct Injection Spray Combustor," Proceedings of ASME GT2006, May 8-11, 2006, Barcelona, Spain.

[8] Legier, J.P., Poinsot, T. and Veynante, D., "Dynamically Thickened Flame LES model for Premixed and Non-premixed Turbulent Combustion," Proceedings of the Summer Program 2000, Center for Turbulence Research, Stanford University, pp. 157-168.

[9] Knudsen, E. and Pitsch, H., "Large Eddy Simulation of a Spray Combustor Using a Multi-regime Flamelet Approach," Annual Research Briefs 2010, Center for Turbulence Research, Stanford University, pp. 337-350.

[10] Sreedhara, S. and Huh, K.Y., "Assessment of Closure Scheme in Second-Order Conditional Moment Closure against DNS with Extinction and Ignition," Combustion and Flame 143 (2005) 386-401.

[11] James, S., Zhu, J. and Anand, M.S., "Large Eddy Simulations of Turbulent Flames Using the Filtered Density Function Model," Proceedings of the Combustion Institute 31 (2007) 1737-1745.

[12] Patel, N., and Suresh, M., "Simulation of Spray-Turbulence-Flame Interactions in a Lean Direct Injection Combustor," Combustion and Flame Vol. 153, 2008, pp. 228-257.

[13] Raju, M.S., "Current Status of the Overall Spray Solution Procedure (Combined CFD/Scalar-Monte-Carlo-PDF/Spray Computations) Developed under NCC," AIAA-2004-0327, 42nd AIAA Aerospace Sciences Meeting and Exhibit, 5-8 January, 2004, Reno, NV.

[14] Shih, T.-H. and Liu, N.-S., "Simulations of Spray Reacting Flows in a Single Element LDI Injector With and Without Invoking an Eulerian Scalar PDF Method," NASA/TM-2012-217676, 2012.

[15] Shih, T.-H. and Liu, N.-S., "Very Large Eddy Simulations of a Jet-A Spray Reacting Flow in a Single Element LDI Injector With and Without Invoking an Eulerian Scalar DWFDF Method," AIAA-2013-2948, 21st Computational Fluid Dynamics Conference, 24-27 June, 2013, San Diego, CA.

[16] Stubbs, R.M. and Liu, N.-S., "Preview of National Combustion Code," AIAA-1997-3114, 33rd AIAA/ASME/SAE/ASEE Joint Conferenc & Exhibit, July 6-9, 1997, Seattle, WA.

[17] Chen, K.-H., Norris, A.T., Quealy, A. and Liu, N.-S., "Benchmark Test Cases for the National Combustion Code," AIAA-1998-3855, 34th AIAA/ASME/SAE/ASEE Joint Propulsion Conference & Exhibit, July 13-15, 1998, Cleveland, OH.

[18] Ryder, R.C., "The Baseline Solver for the National Combustion Code," AIAA-1998-3853, 34th AIAA/ASME/SAE/ASEE Joint Propulsion Conference & Exhibit, July 13-15, 1998, Cleveland, OH.

[19] Ajmani, K. and Chen, K.-H., "Unsteady-Flow Computations for the NCC," AIAA-2001-0972, 39th AIAA Aerospace Sciences Meeting & Exhibit, 8-11 January, 2001, Reno, NV.

[20] Liu, N.-S., "On the Comprehensive Modeling and Simulation of Combustion Systems," AIAA-2001-0805, 39th AIAA Aerospace Sciences Meeting & Exhibit, 8-11 January, 2001, Reno, NV.

[21] Quealy, A., "National Combustion Code Parallel Performance Enhancements," 38th AIAA/ASME/SAE/ASEE Joint Propulsion Conference and Exhibit, July 7-10, 2002, Indianapolis, IN.

[22] Liu, N.-S. and Chen, K.-H., "An Alternative Flow Solver for the NCC – The FLUX Code and its Algorithm," AIAA-2001-0973, 39th AIAA Aerospace Sciences Meeting & Exhibit, 8-11 January, 2001, Reno, NV.

[23] Cai, J., Jeng, S.-M., and Tacina, R., "The Structure of a Swirl-Stabilized Reacting Spray Issued from an Axial Swirler," AIAA-2005-1424, 43rd AIAA Aerospace Science Meeting and Exhibit, 10-13 January, 2005, Reno, NV.

[24] Shih, T.-H. and Liu, N-S., "Numerical Study of Outlet Boundary Conditions for Unsteady Turbulent Internal Flows Using the NCC," NASA/TM-2009-215486, 2009.

[25] Shih, T.-H., Povinelli, L.A., Liu, N.-S. and Chen, K.-H., "Generalized Wall Function for Complex Turbulent Flows," NASA/TM-2000-209936, 2000.

[26] Iannetti, A.C. and Liu, N.-S., "The Effect of Spray Initial Conditions on Heat Release and Emissions in LDI CFD Calculations," AIAA-2008-1150, 46th AIAA Aerospace Science Meeting and Exhibit, 7-10 January, 2008, Reno, NV.

[27] Iannetti, A.C. and Moder, J.P., "Comparing Spray Characteristics from RANS NCC Calculations Against Experimental Data for a Turbulent Reacting Flow," AIAA-2010-578, 48th AIAA Aerospace Sciences Meeting, 4-7 January, 2010, Orlando, FL.

[28] Liu, N.-S. and Shih, T.-H., "A Very Large Eddy Simulation of the Non-reacting Flow in a Single-Element Lean Direct Injection Combustor Using PRNS with a Nonlinear Subscale Model," ISROMAC-13-36, Proceedings of the 13th International Symposium on Transport Phenomena and Dynamics of Rotating Machinery, 4-9 April, 2010, Honolulu, HI.

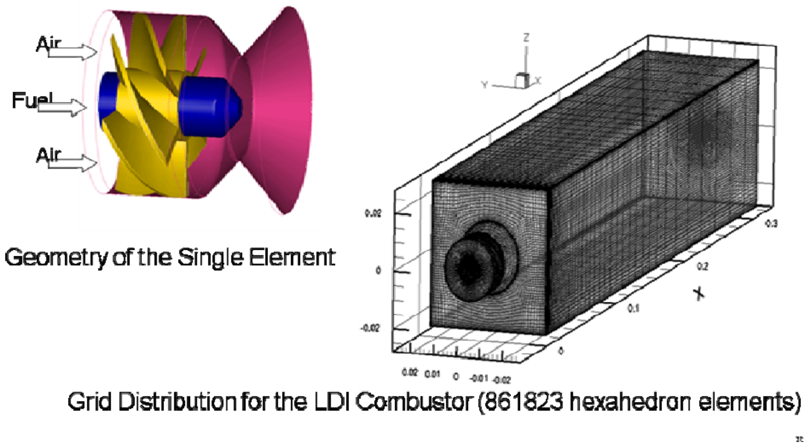

Geometry of the Single Element

Grid Distribution for the LDI Combustor (861823 hexahedron elements)

Figure 3. Swirler geometry and computational domain of a single-element LDI combustor.

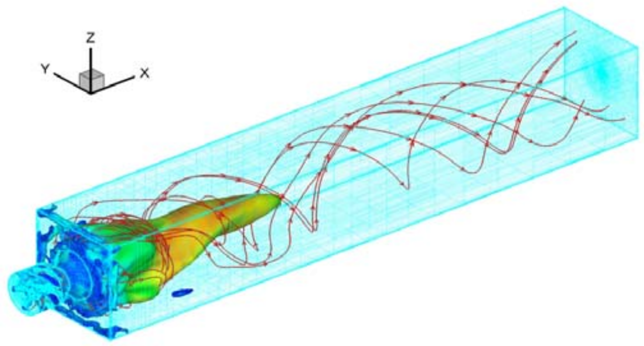

Figure 4. A snapshot of the unsteady flow field.

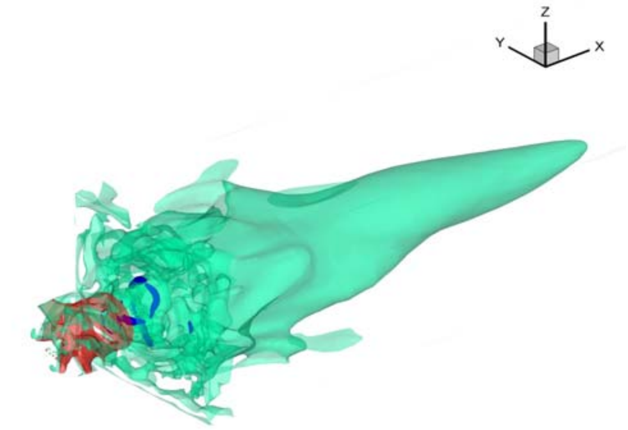

Figure 5. A snapshot of the precessing-vortex core (PVC) and the vortex-breakdown bubble (VBB).

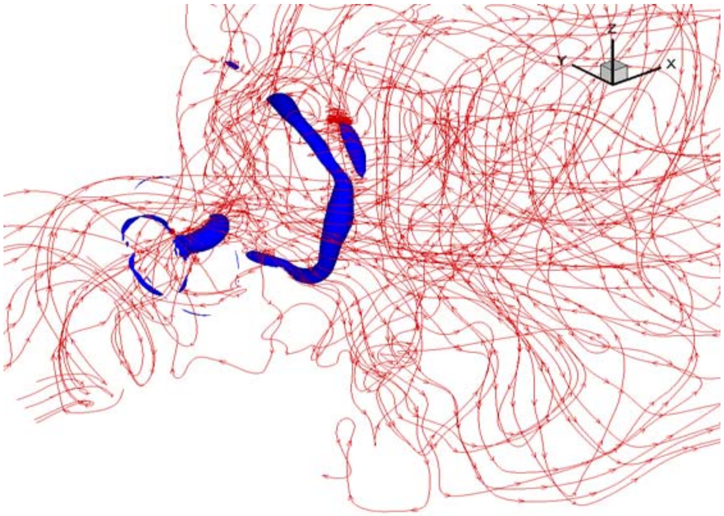

Figure 6. Instantaneous streamlines around the precession vortex core (PVC).

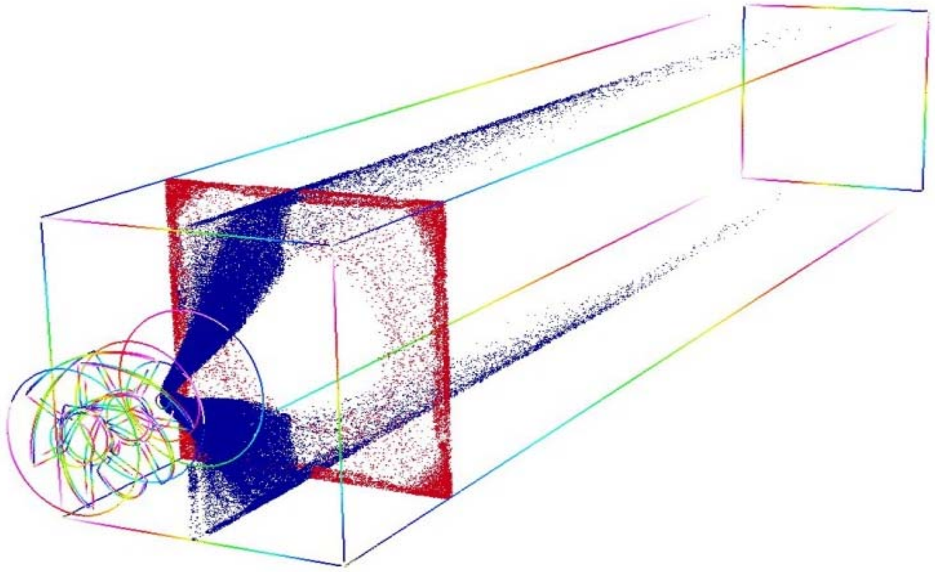

Figure 7. A snapshot of the fuel-droplet distribution in the center plane and a cross-section.

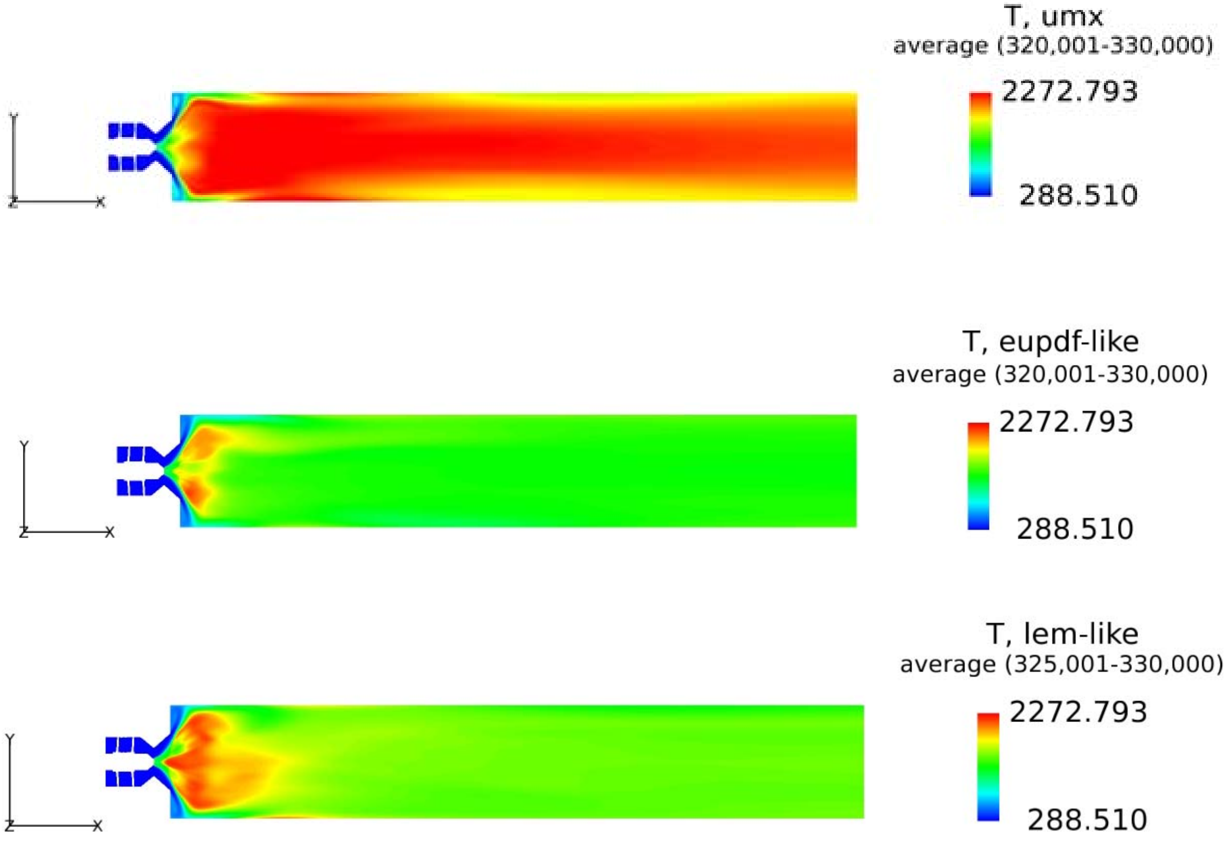

Figure 8. Comparison of subgrid models: temperature field in the center plane (z=0).

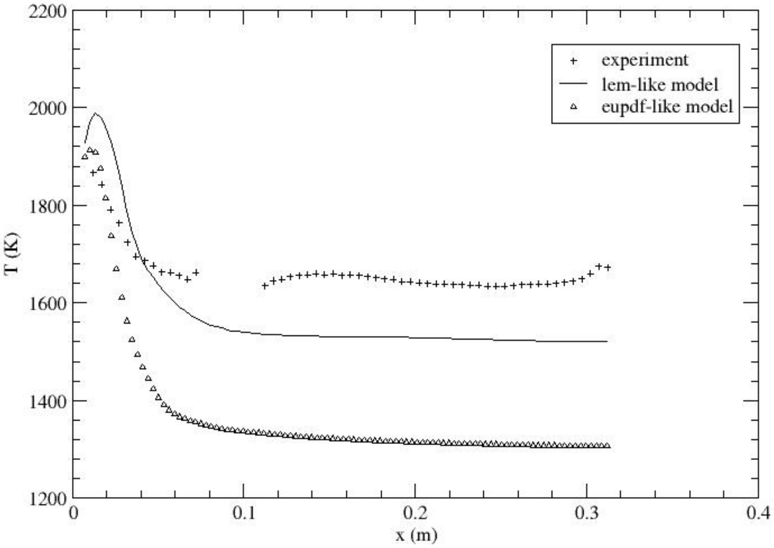

Figure 9. Averaged temperature along the center line.

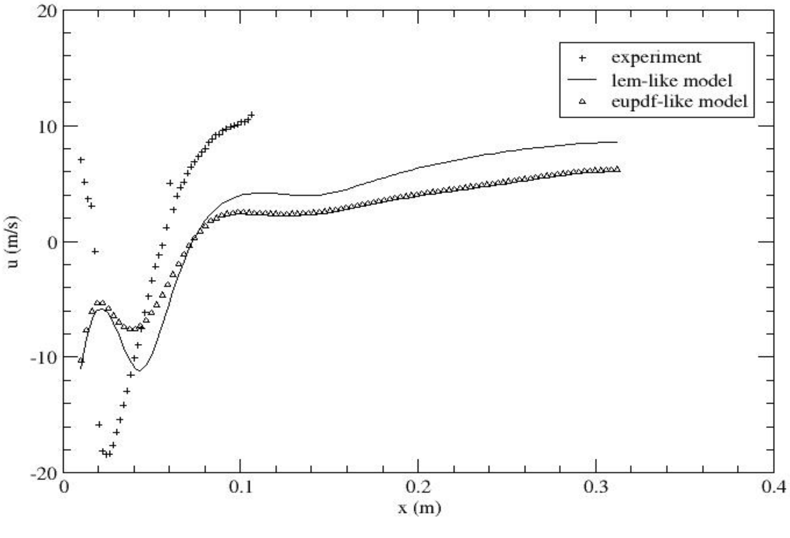

Figure 10. Averaged axial velocity along the center line.

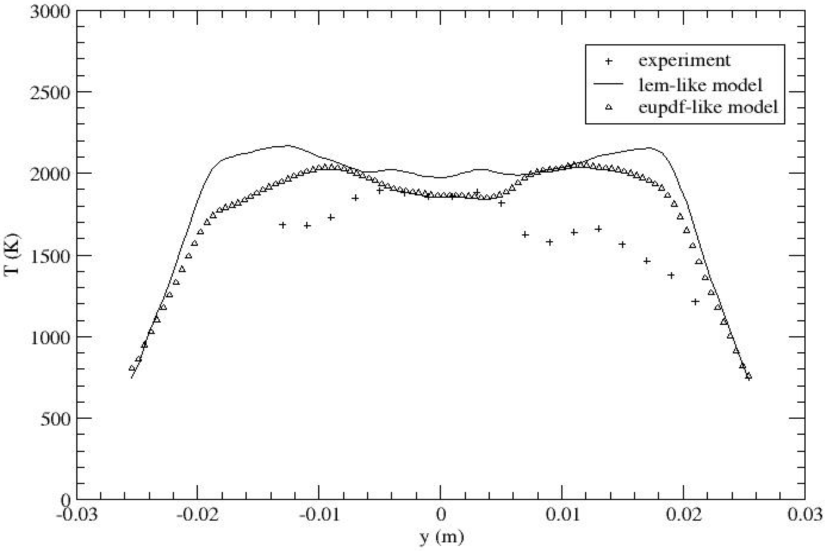

Figure 11. Radial profile of averaged temperature (10 mm downstream of the dump plane).

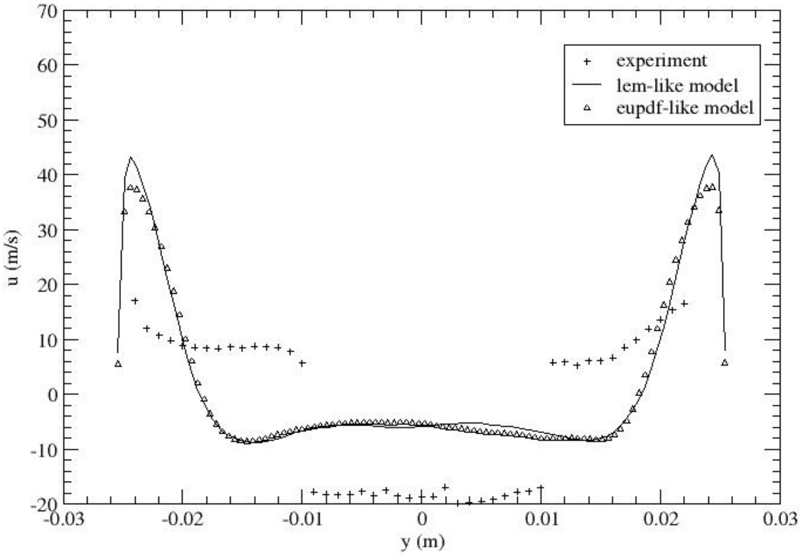

Figure 12. Radial profile of averaged axial velocity (15 mm downstream of the dump plane).

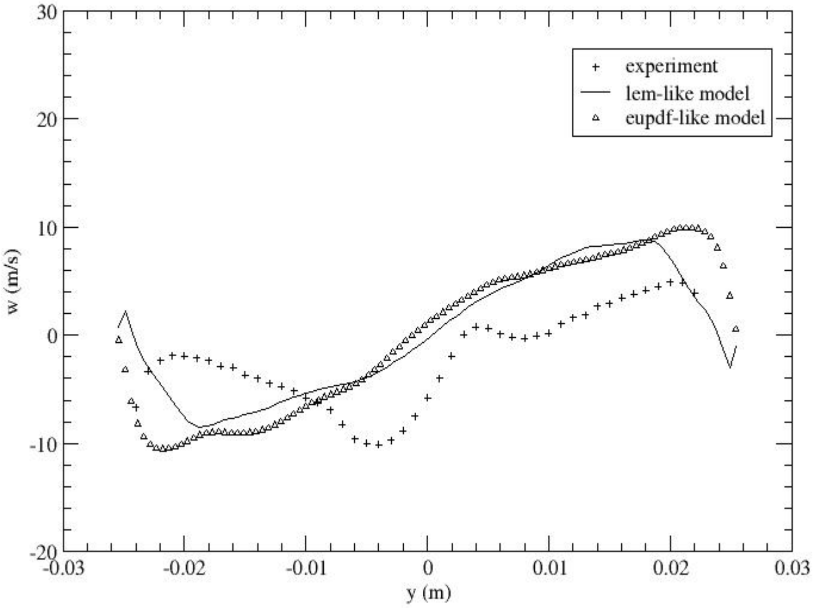

Figure 13. Radial profile of averaged azimuthal velocity (15 mm downstream of the dump plane).

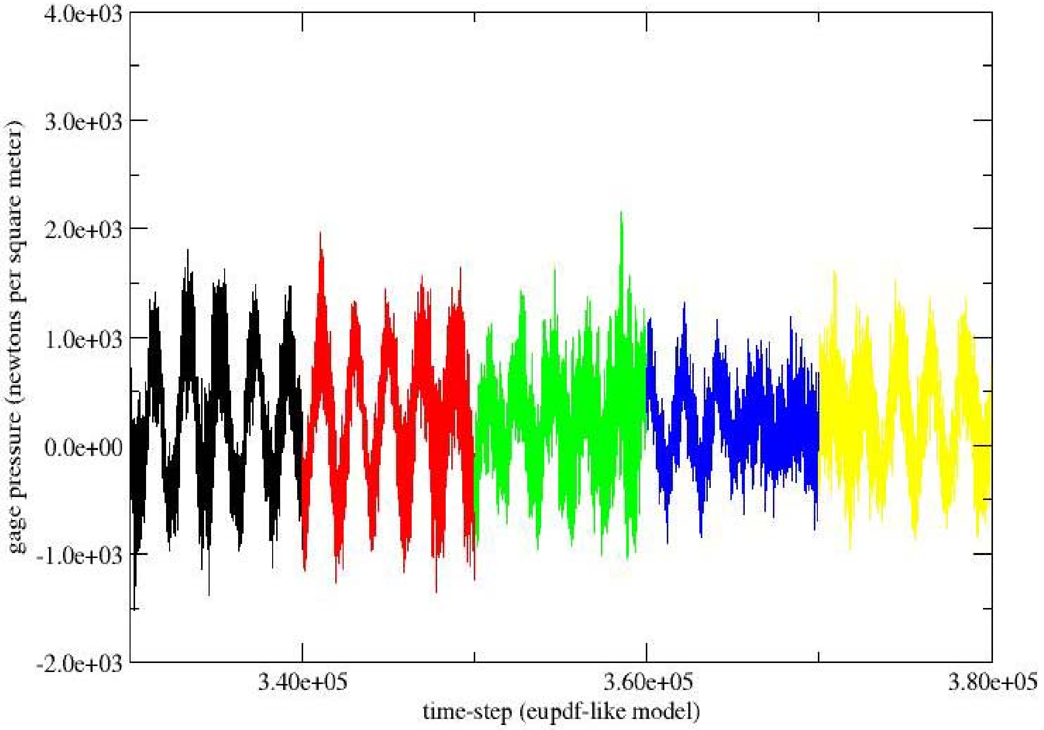

Figure 14. Pressure history at a center point which is 7.8 mm downstream of the dump plane.

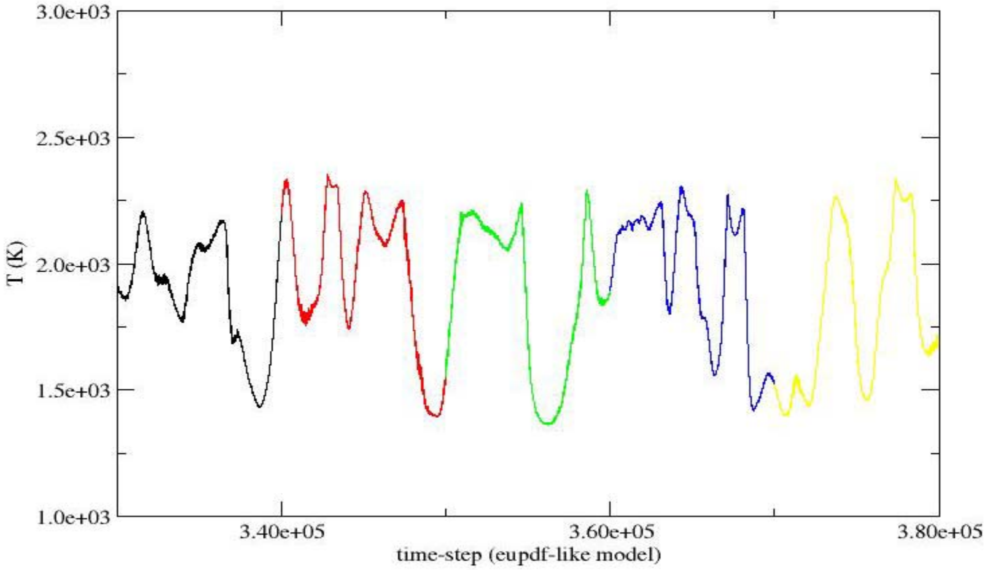

Figure 15. Temperature history at a center point which is 7.8 mm downstream of the dump plane.

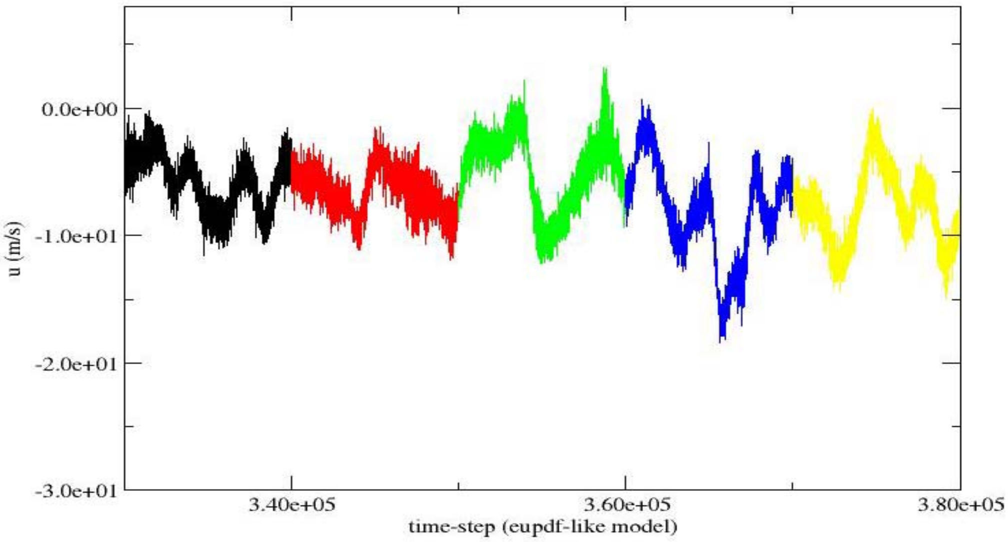

Figure 16. Axial velocity history at a center point which is 7.8 mm downstream of the dump plane.

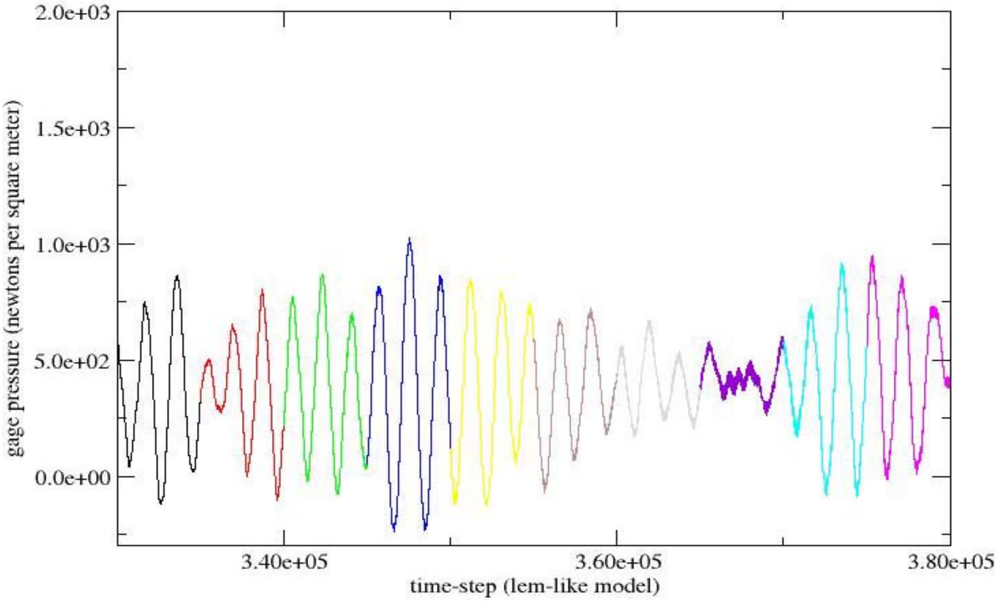

Figure 17. Pressure history at a center point which is 7.8 mm downstream of the dump plane.

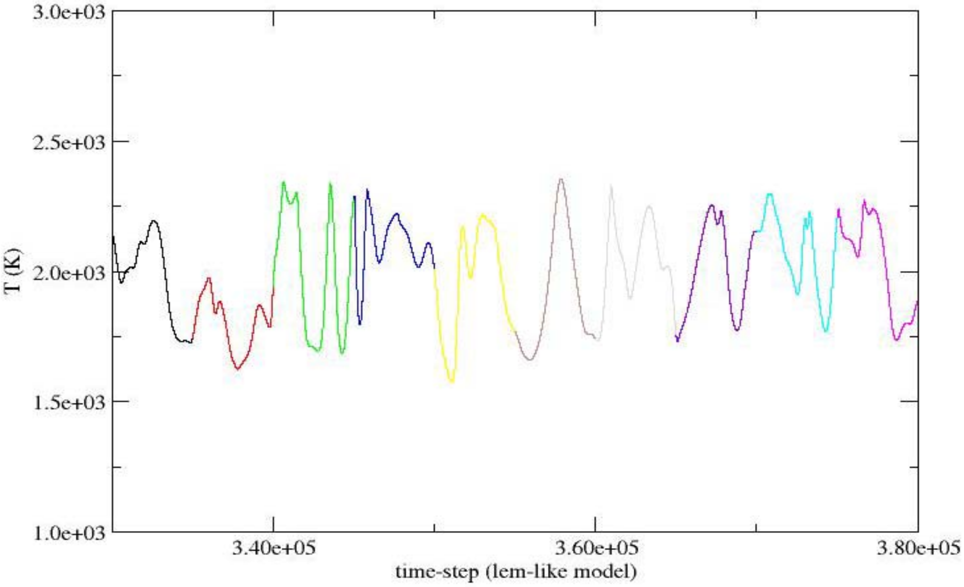

Figure 18. Temperature history at a center point which is 7.8 mm downstream of the dump plane.

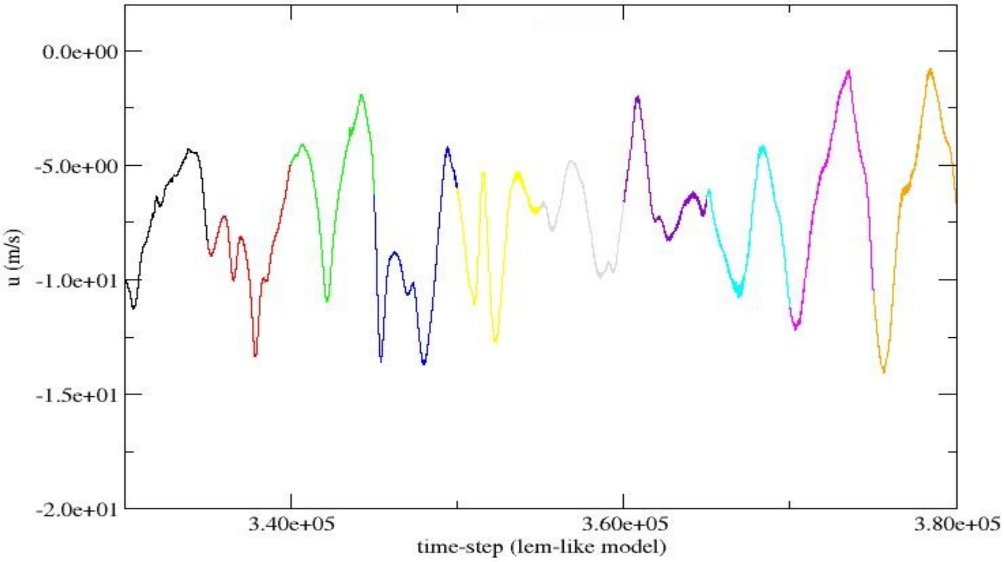

Figure 19. Axial velocity history at a center point which is 7.8 mm downstream of the dump plane.

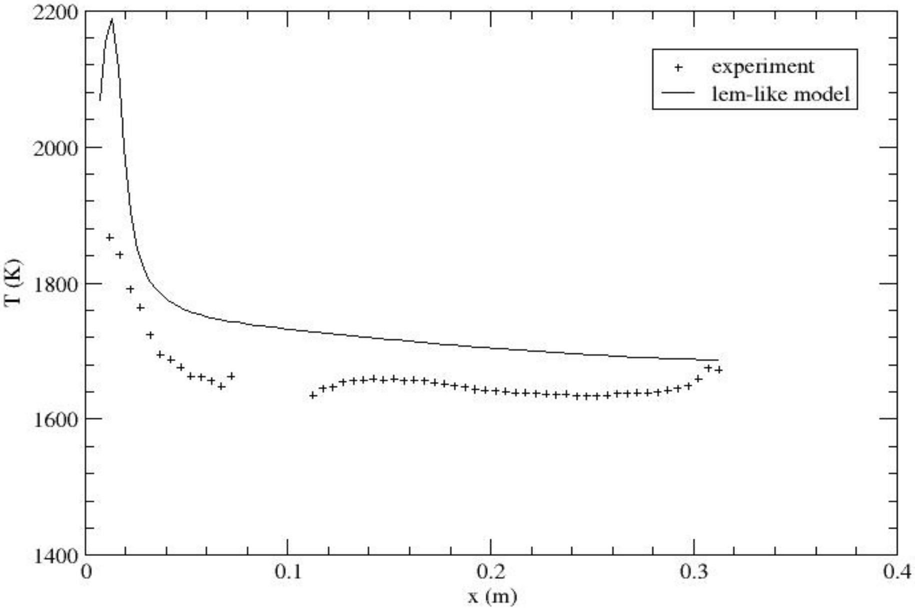

Figure 20. Averaged temperature along the center line.

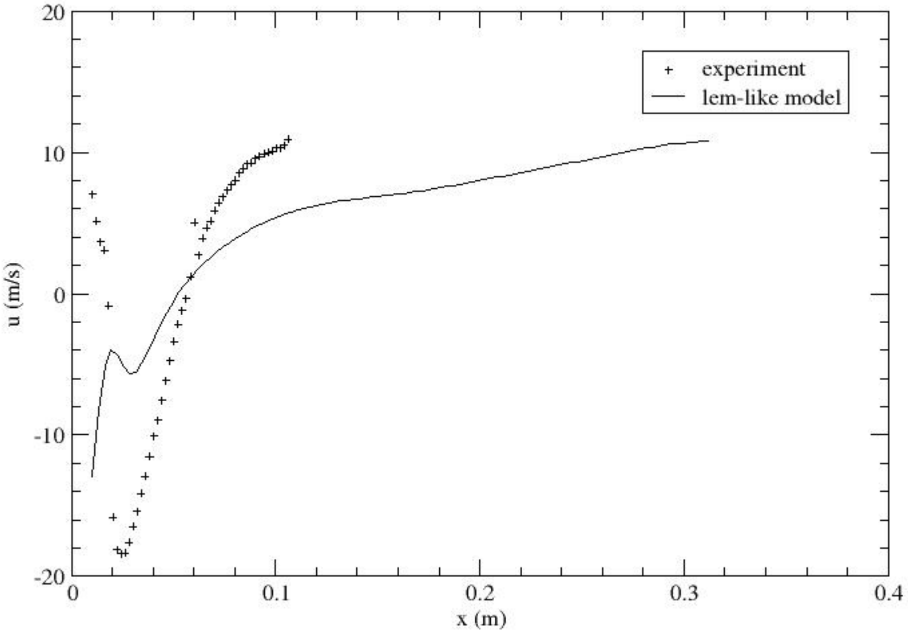

Figure 21. Averaged axial velocity along the center line.

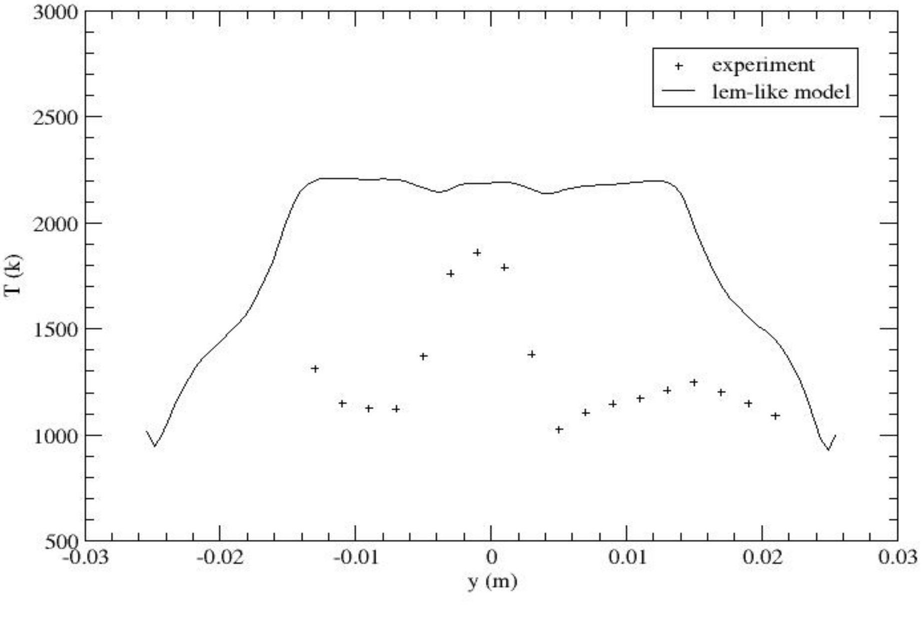

Figure 22. Radial profile of averaged temperature (5 mm downstream of the dump plane).

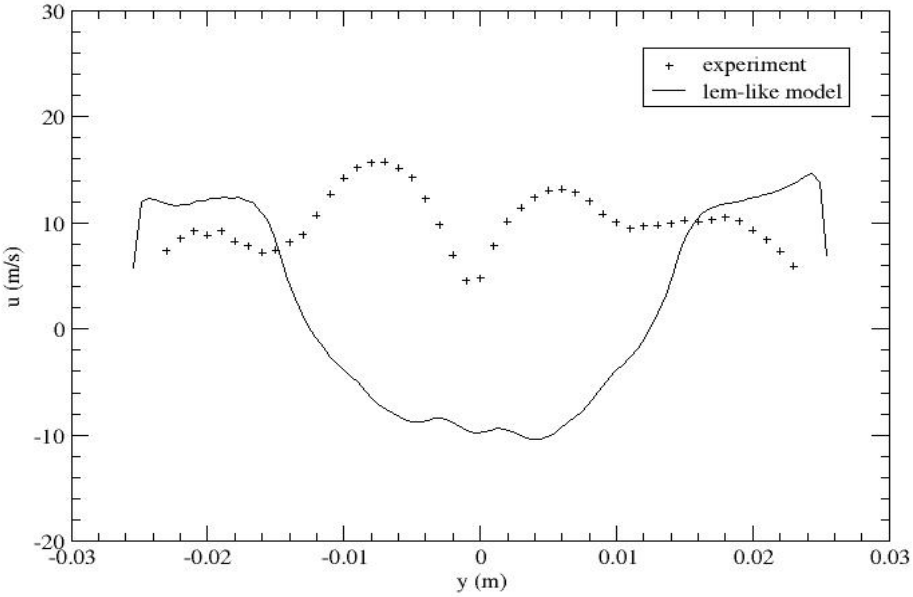

Figure 23. Radial profile of averaged axial velocity (5 mm downstream of the dump plane).

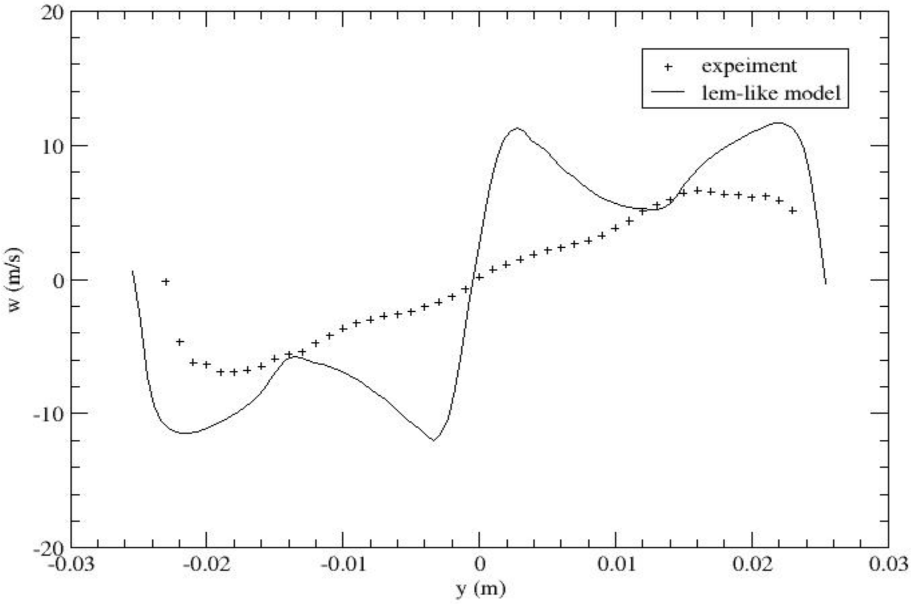

Figure 24. Radial profile of averaged azimuthal velocity (5 mm downstream of the dump plane).

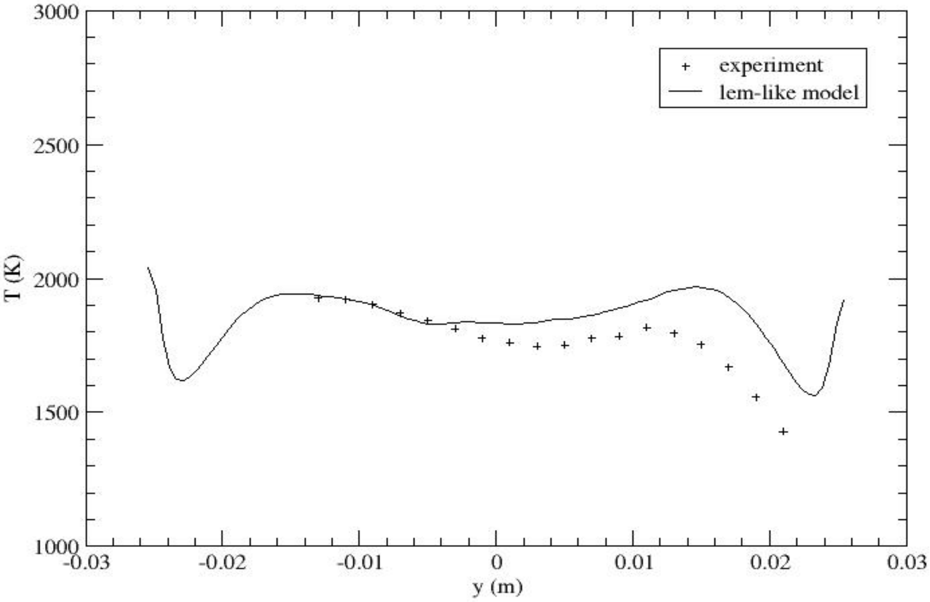

Figure 25. Radial profile of averaged temperature (20 mm downstream of the dump plane).

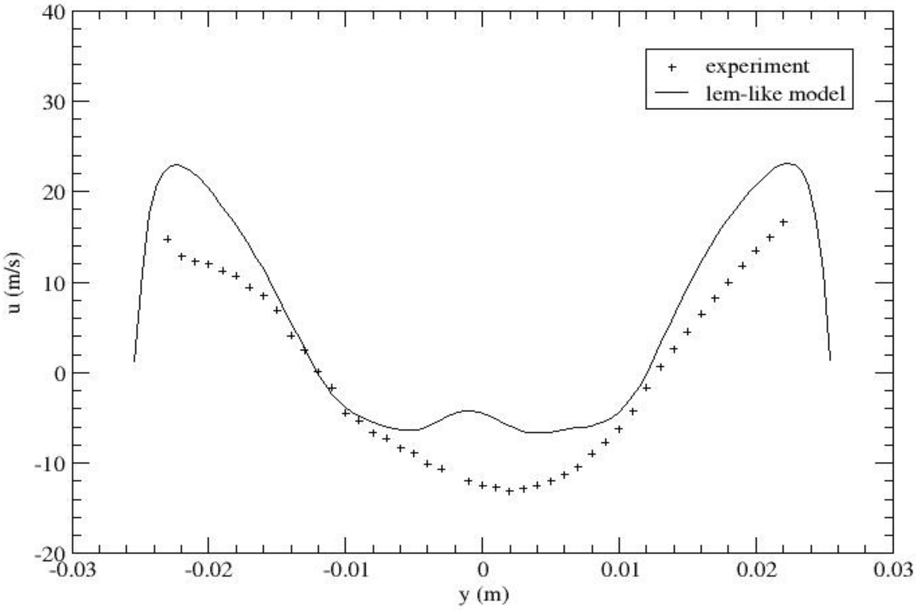

Figure 26. Radial profile of averaged axial velocity (29 mm downstream of the dump plane).

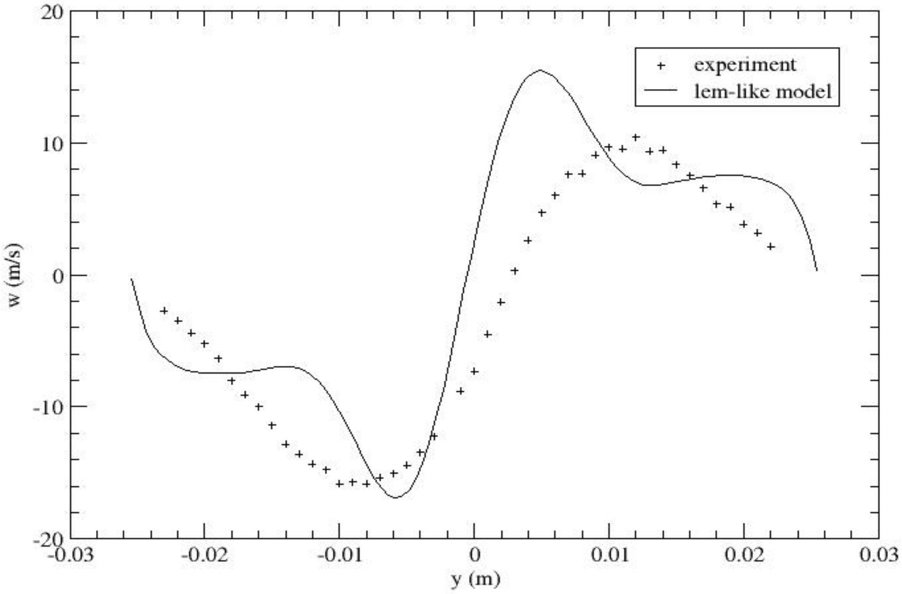

Figure 27. Radial profile of averaged azimuthal velocity (29 mm downstream of the dump plane).

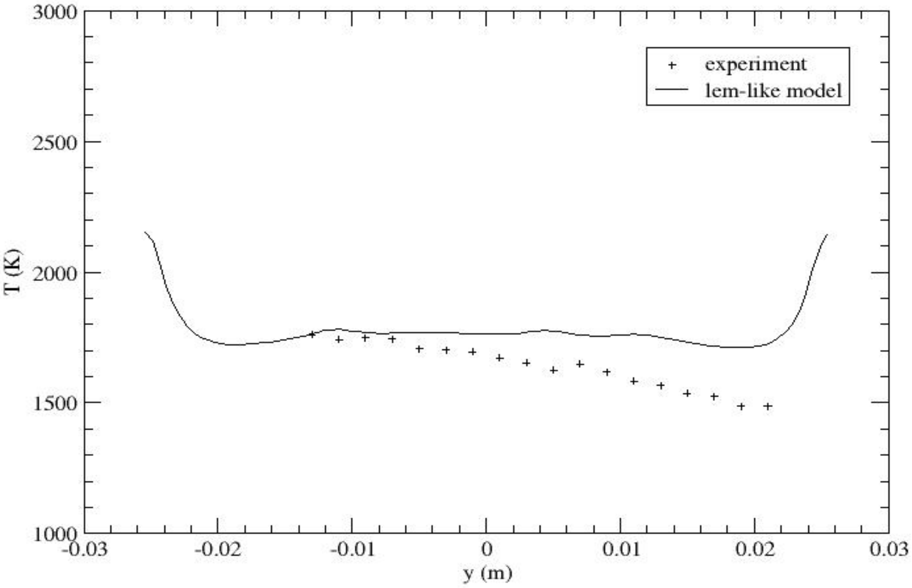

Figure 28. Radial profile of averaged temperature (40 mm downstream of the dump plane).

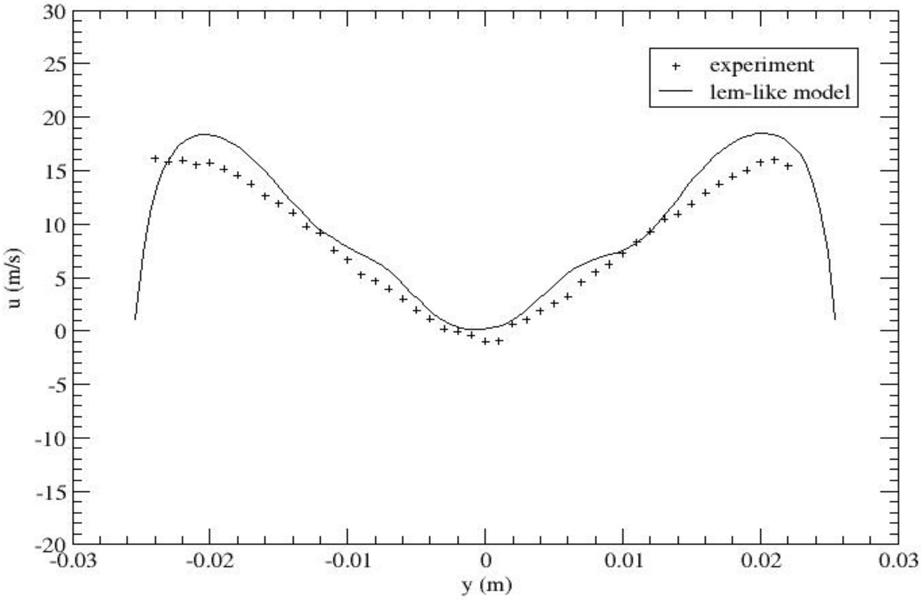

Figure 29. Radial profile of averaged axial velocity (46 mm downstream of the dump plane).

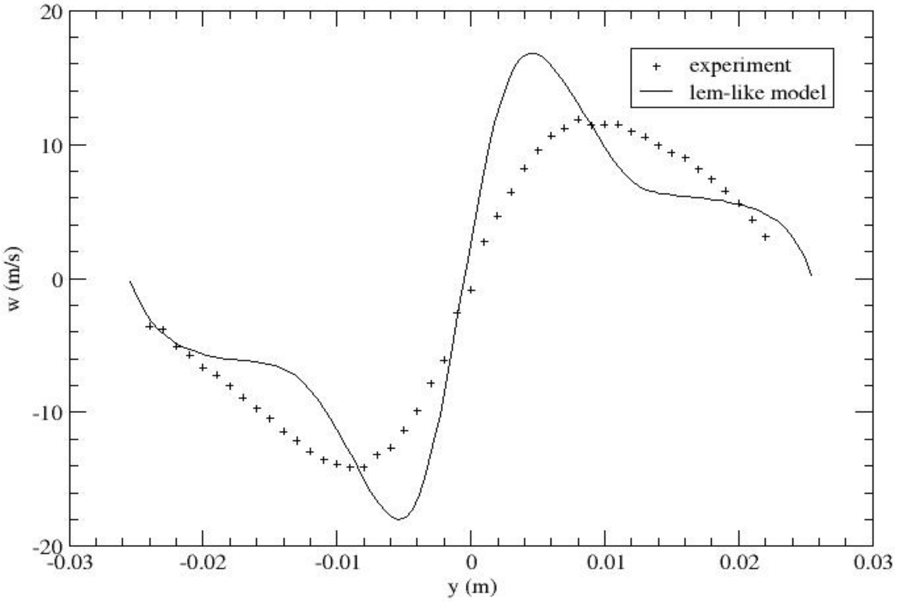

Figure 30. Radial profile of averaged azimuthal velocity (46 mm downstream of the dump plane).

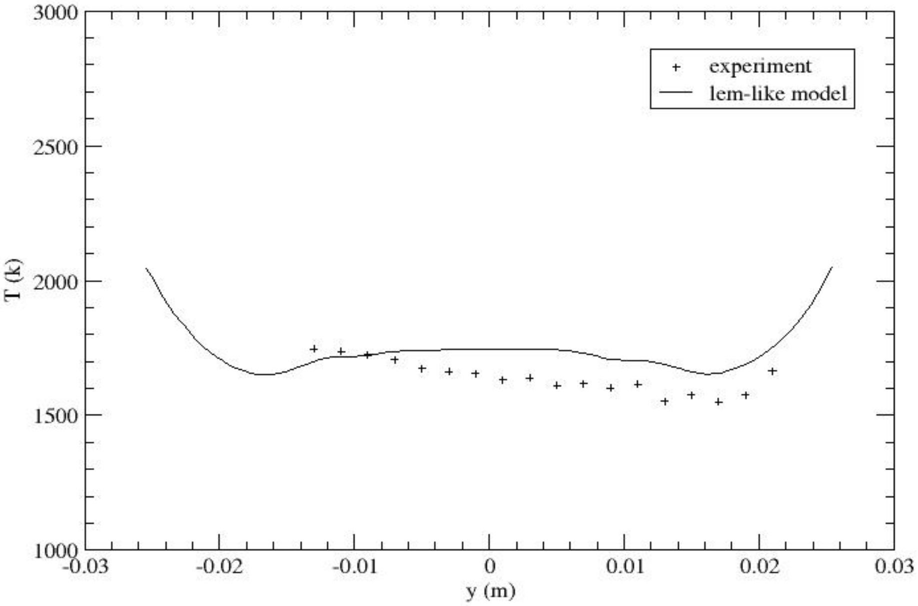

Figure 31. Radial profile of averaged temperature (60 mm downstream of the dump plane).

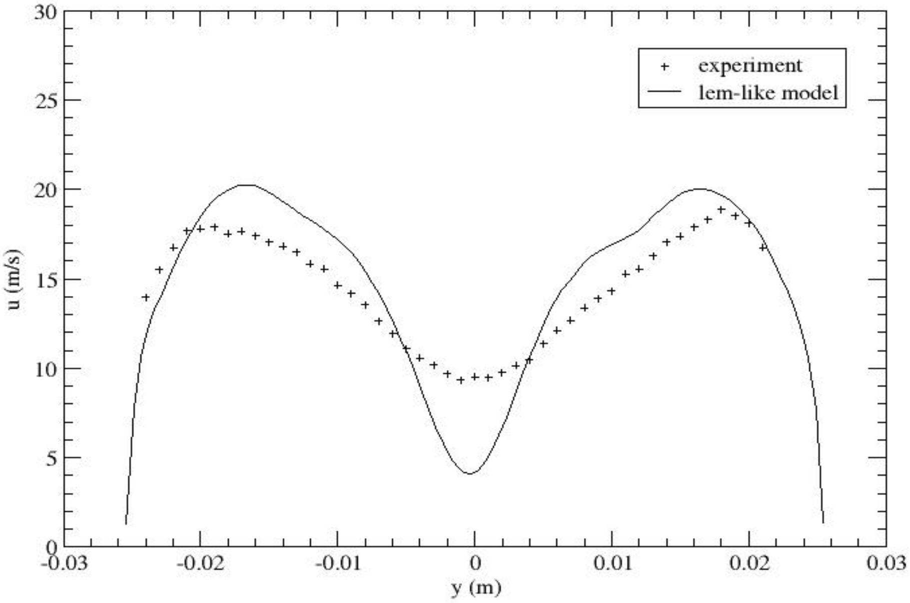

Figure 32. Radial profile of averaged axial velocity (76 mm downstream of the dump plane).

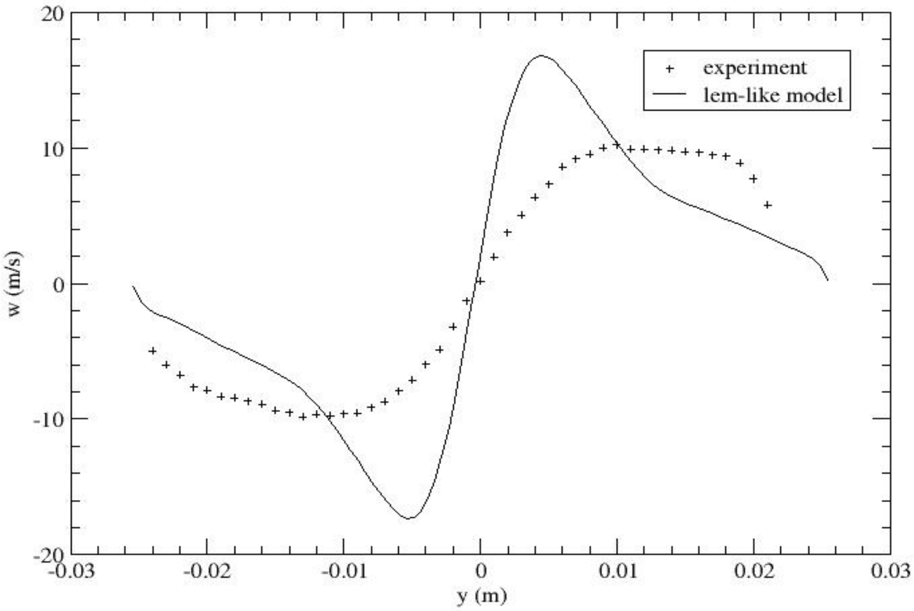

Figure 33. Radial profile of averaged azimuthal velocity (76 mm downstream of the dump plane).

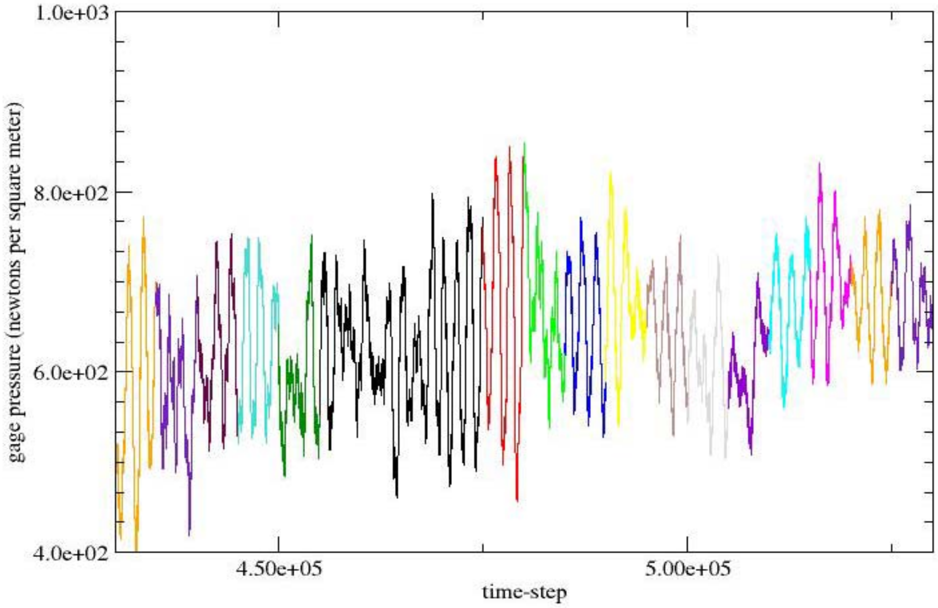

Figure 34. Pressure history at a center point which is 7.8 mm downstream of the dump plane.

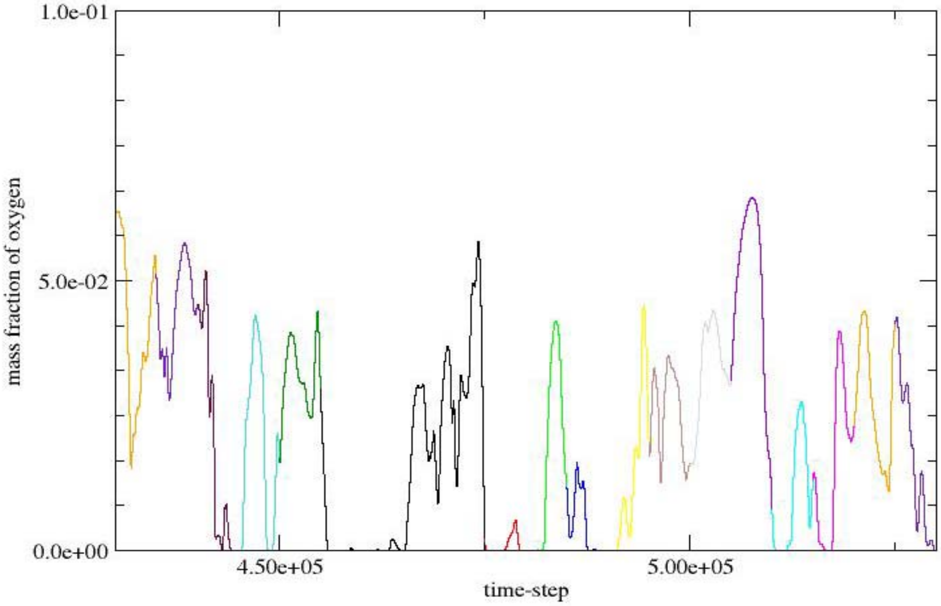

Figure 35. Oxidizer history at a center point which is 7.8 mm downstream of the dump plane.

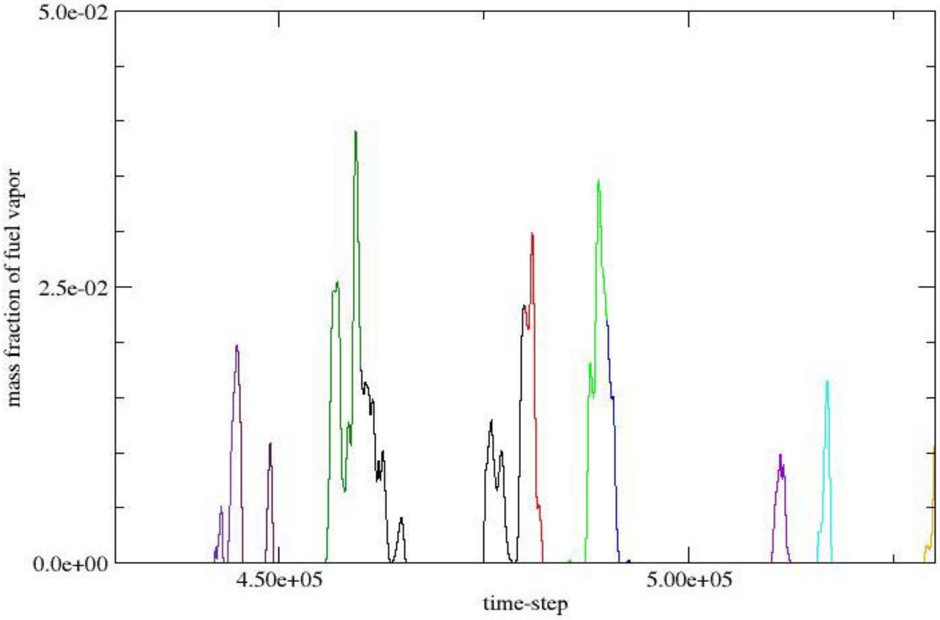

Figure 36. Fuel vapor history at a center point which is 7.8 mm downstream of the dump plane.

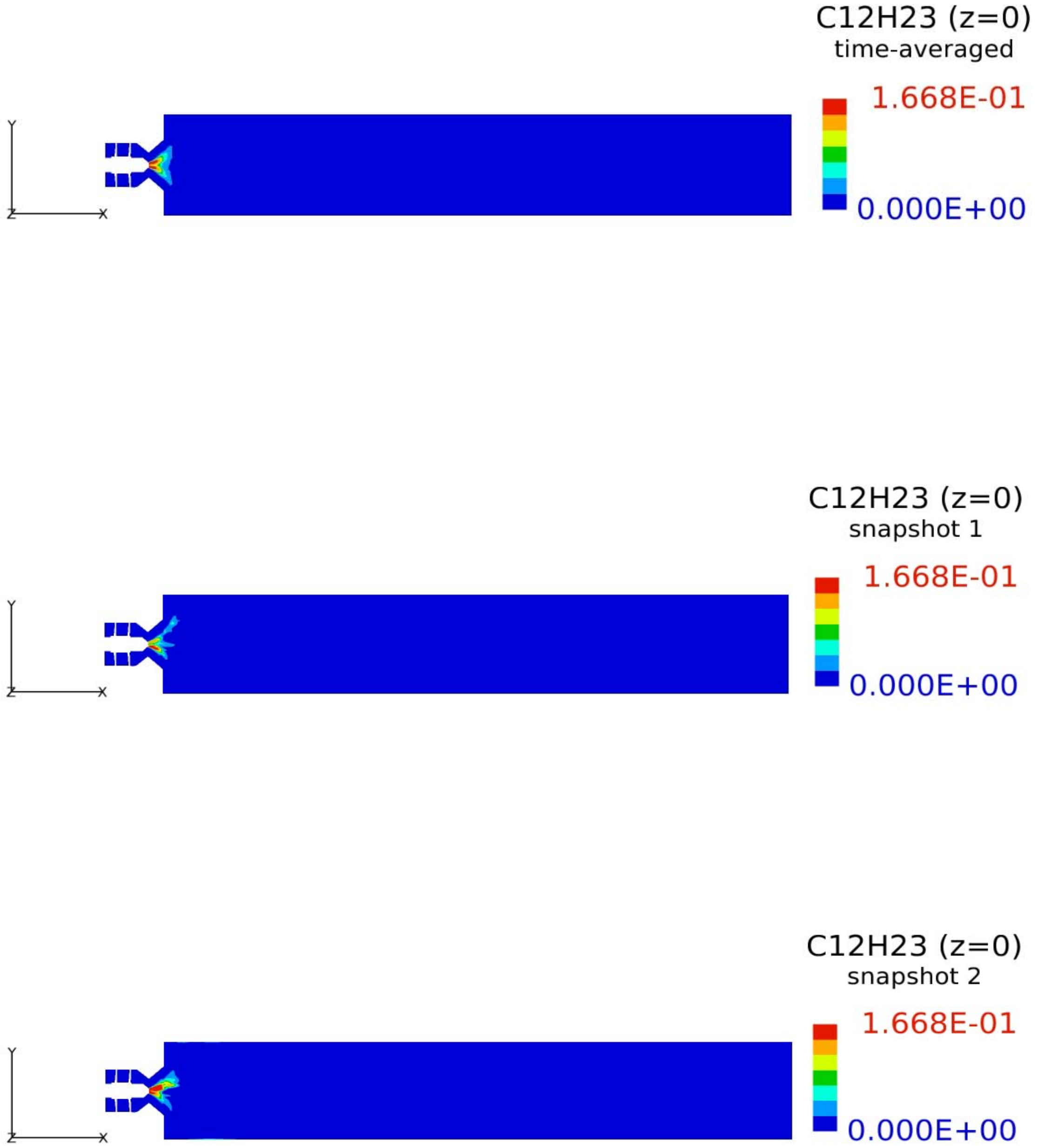

Figure 37. Fuel vapor distribution in the center plane: time-averaged field and two snapshots.

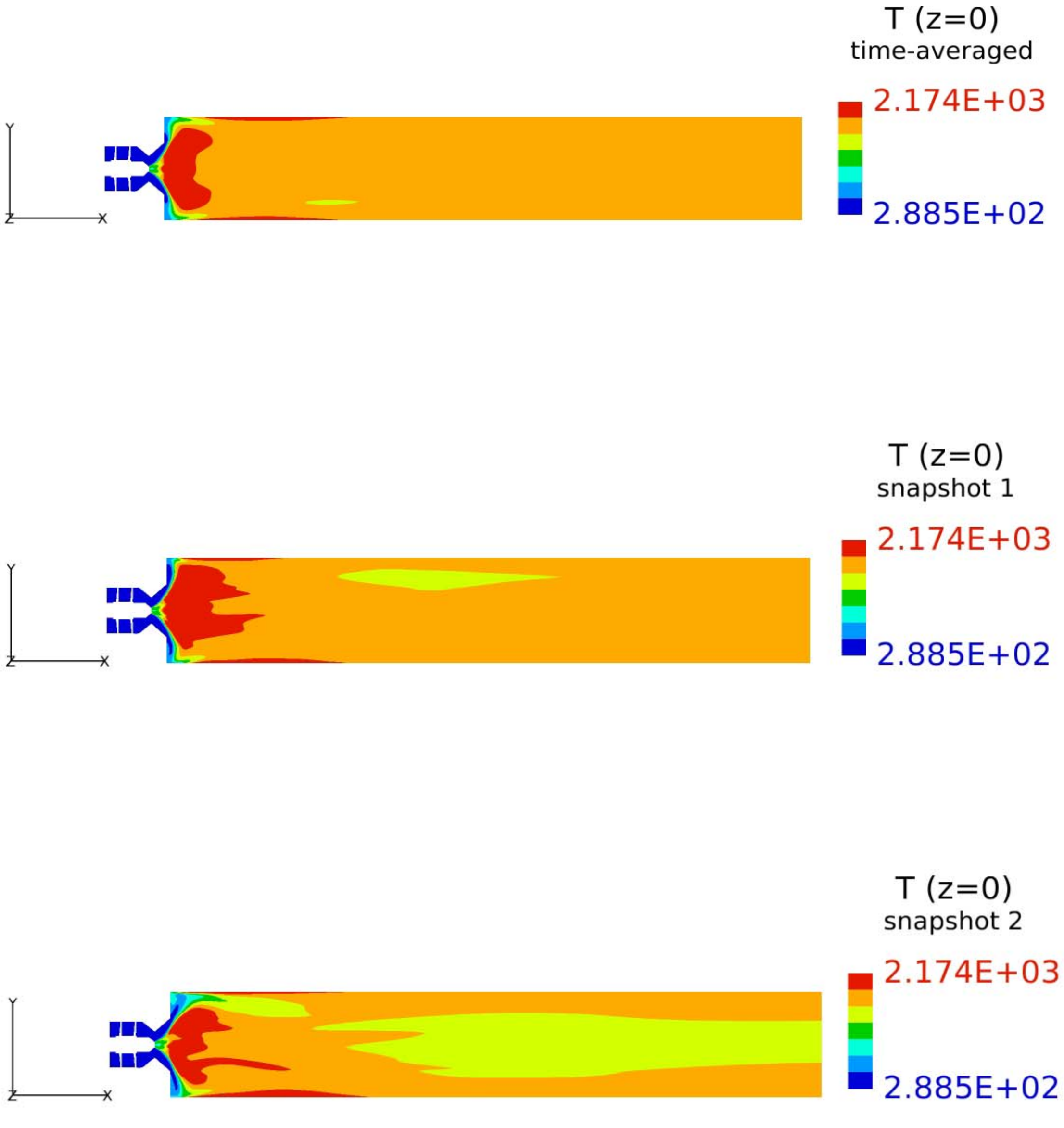

Figure 38. Temperature distribution in the center plane: time-averaged field and two snapshots.